

 Open access • Journal Article • DOI:10.1007/S10712-019-09508-0

High-Resolution Characterization of Near-Surface Structures by Surface-Wave Inversions: From Dispersion Curve to Full Waveform — [Source link](#)





Yudi Pan, Lingli Gao, Thomas Bohlen

Institutions: Karlsruhe Institute of Technology

Published on: 01 Mar 2019 - Surveys in Geophysics (Springer Netherlands)

Related papers:

- [Estimation of near-surface shear-wave velocity by inversion of Rayleigh waves](#)
- [Multichannel analysis of surface waves](#)
- [Application of a complete workflow for 2D elastic full-waveform inversion to recorded shallow-seismic Rayleigh waves](#)
- [Surface-wave analysis for building near-surface velocity models — Established approaches and new perspectives](#)
- [Sinkhole detection using 2D full seismic waveform tomography](#)

Share this paper:    

View more about this paper here: <https://typeset.io/papers/high-resolution-characterization-of-near-surface-structures-2f42ljv5um>

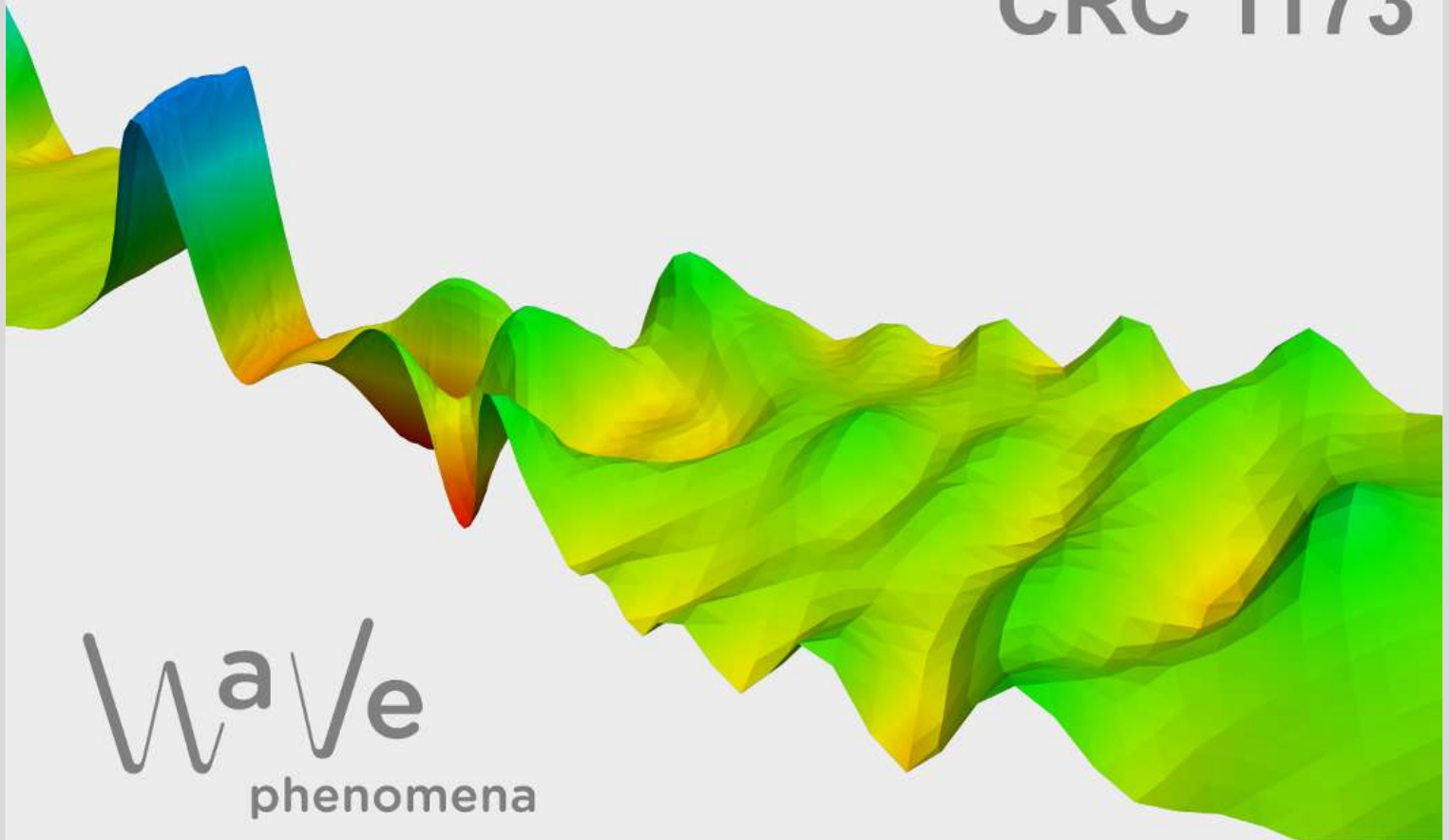
High-resolution characterization of near-surface structures by surface-wave inversions: From dispersion curve to full waveform

Yudi Pan, Lingli Gao, Thomas Bohlen

CRC Preprint 2019/3, January 2019

KARLSRUHE INSTITUTE OF TECHNOLOGY

CRC 1173



Participating universities



Universität Stuttgart

EBERHARD KARLS
UNIVERSITÄT
TÜBINGEN



Funded by

DFG

ISSN 2365-662X

High-resolution characterization of near-surface structures by surface-wave inversions: From dispersion curve to full waveform

Yudi Pan · Lingli Gao · Thomas Bohlen

Received: 07.Jan.2019

Abstract Surface waves are widely used in near-surface geophysics and provide a non-invasive way to determine near-surface structures. By extracting and inverting dispersion curves to obtain local 1D S-wave velocity profiles, multichannel analysis of surface waves (MASW) has been proven as an efficient way to analyze shallow-seismic surface waves. By directly inverting the observed waveforms, full-waveform inversion (FWI) provides another feasible way to use surface waves in reconstructing near-surface structures. This paper provides a state of the art on MASW and shallow-seismic FWI, and a comparison of both methods. A two-parameter numerical test is performed to analyze the nonlinearity of MASW and FWI, including the classical, the multiscale, the envelope-based, and the amplitude-spectrum-based FWI approaches. A checkerboard model is used to compare the resolution of MASW and FWI. These numerical examples show that classical FWI has the highest nonlinearity and resolution among these methods, while MASW has the lowest nonlinearity and resolution. The modified FWI approaches have an intermediate nonlinearity and resolution between classical FWI and MASW. These features suggest that a sequential application of MASW and FWI could provide an efficient hierarchical way to delineate near-surface structures. We apply the sequential-inversion strategy to two field data sets acquired in Olathe, Kansas, USA, and Rheinstetten, Germany, respectively. We build a 1D initial model by using MASW and then apply the multiscale FWI to the data. High-resolution 2D S-wave velocity images are obtained in both cases, whose reliabilities are proven by borehole data and a GPR profile, respectively. It demonstrates the effectiveness of combining MASW and FWI for high-resolution imaging of near-surface structures.

Keywords MASW · FWI · Surface waves · Shallow seismic · Dispersion curve · Shear-wave velocity

1 Introduction

The reconstruction of near-surface elastic-parameter models is of fundamental importance for near-surface geophysical and geotechnical studies. Surface waves dominate the shallow-seismic wavefield and are attractive for determining near-surface structures due to their relatively high signal-to-noise ratio in field recordings. With a rapid development in the theories of surface-wave methods, it has become increasingly popular over the last two decades to use surface waves as a non-invasive way to estimate near-surface structures.

The analysis of shallow-seismic surface waves started with the spectral analysis of surface waves (SASW; [Nazarian et al 1983](#)), and prospered after the introduction of multichannel analysis of surface waves (MASW; [Park et al 1999](#); [Xia et al 1999](#)), which greatly improved the efficiency of surface-wave surveys by using a multistation approach. Both SASW and MASW use the dispersion characteristic of surface waves to determine near-surface structures, and a comparison of their performances is presented in [Lin et al \(2017\)](#). Two main steps in MASW are the extraction and the inversion of the surface-wave dispersion curve (upper part in Fig. 1), which will be introduced in detail hereafter. Thus, many efforts have been made to improve the accuracy of surface-wave dispersion images (e.g., [Park et al 1998](#); [Forbriger 2003](#); [Lin and Chang 2004](#); [Xia et al 2007](#); [Parolai 2009](#); [Askari and Hejazi 2015](#); [Shen et al 2015](#); [Mun et al 2015](#); [Verachtert et al 2017](#);

Y. Pan and T. Bohlen
Geophysical Institute, Karlsruhe Institute of Technology (KIT), Karlsruhe, Germany
E-mail: yudi.pan@kit.edu; thomas.bohlen@kit.edu

L. Gao
Department of Mathematics, Karlsruhe Institute of Technology (KIT), Karlsruhe, Germany
E-mail: lingli.gao@kit.edu

Kumar and Naskar 2017) and to reduce the nonuniqueness of the inverse problem (e.g., Xia et al 1999, 2003; Ivanov et al 2006; Lu et al 2007; Socco and Boiero 2008; Cercato 2009; Maraschini and Foti 2010). Several reviews of MASW can be found in Socco et al (2010), Foti et al (2011), Xia (2014) and Garofalo et al (2016).

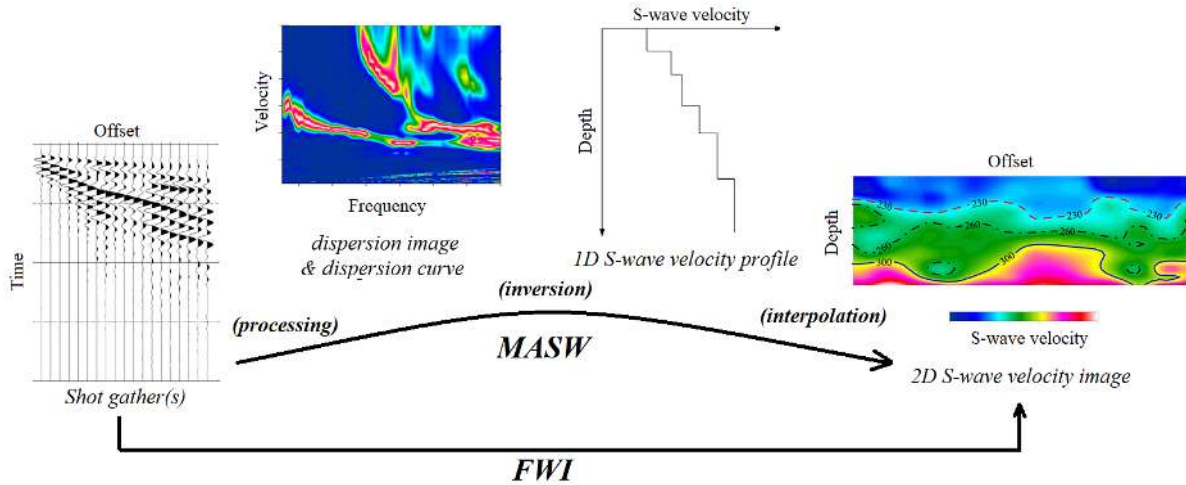


Fig. 1 Comparison of the workflows of multichannel analysis of surface waves (MASW) and full-waveform inversion (FWI).

Based on phase-velocity inversion, MASW allows the reconstruction of S-wave velocity as a function of depth. Different approaches have been proposed to account for lateral heterogeneity, such as cross-correlation analysis of multichannel data (Hayashi and Suzuki 2004; Ikeda et al 2013), spatial filtering (Bohlen et al 2004; Bergamo et al 2012), and laterally constrained inversion (Socco et al 2009). These approaches account for the 2D effect in MASW (Di Fiore et al 2016) and make MASW applicable to not only layered but also laterally smoothly varying models. Due to the 1D layered model and the plane wave assumptions involved in the forward calculation of surface-wave dispersion curves, however, methods based on dispersion curves fail to work when strong lateral heterogeneity exists, which is regarded as one of the limitations in MASW. Another problem faced with MASW is the difficulty in the correct estimation and identification of multimodal dispersion curves (Zhang and Chan 2003; Boaga et al 2013; Gao et al 2014), especially when encountering low-velocity layers (Tsuji et al 2012; Pan et al 2013a; Mi et al 2018), strong vertical contrasts (De Nil 2005; Renalier et al 2010; Gao et al 2016), and a non-planar free surface (Zeng et al 2012; Wang et al 2015).

With a rapid increase in computational power, it has become feasible to use full-waveform inversion (FWI; Tarantola 1986, 1988, 2005) to resolve a subsurface model by fitting the observed waveform directly (lower part in Fig. 1). Based on full-wavefield modeling, FWI is able to fully exploit the waveform information and is getting increasingly popular on continental (Fichtner et al 2008), explorational (Virieux and Operto 2009), near-surface (Groos et al 2017), and laboratory (Köhn et al 2016) scales. Due to the specific wavefield characteristics (e.g., frequency range and wave type) and recording systems in each scale, the successful application of FWI on different scales is not simply a matter of scale. For example, due to the existence of surface waves, the acoustic approximation, which is widely adopted in explorational seismics, is no longer valid in shallow seismics. The inclusion of surface waves in the wavefields also increases the nonlinearity of FWI (Gélis et al 2007; Brossier et al 2009). Numerical examples (Romdhane et al 2011; Zeng et al 2011a; Breteau et al 2013; Borisov et al 2017; Pan et al 2018a) have demonstrated that FWI is a promising way in quantitatively imaging near-surface structures. Applications of FWI on field data sets (Tran et al 2013; Kallivokas et al 2013; Amrouche and Yamanaka 2015; Nguyen et al 2016; Pan et al 2016b; Dokter et al 2017) have also proved the applicability as well as the high resolution of FWI for characterizing near-surface heterogeneity. Shallow-seismic FWI is an ill-posed problem and could converge toward a local minimum especially when a poor initial model is provided (Virieux and Operto 2009). An effective way to reduce the ambiguity of shallow-seismic FWI is to use an appropriate initial model provided by MASW (Pan et al 2017). Another way to mitigate its ill-posedness of shallow-seismic FWI is the smart design of the objective function, such as multiscale FWI (MFWI; Bunks et al 1995; Groos et al 2017), envelope-based FWI (EFWI; Bozdağ et al 2011; Wu et al 2014), and amplitude-spectrum-based FWI (AFWI; Pérez Solano et al 2014; Dou and Ajo-Franklin 2014).

Unlike MASW which only uses the averaged phase velocity of multichannel data and exploits the general part in the phase information of surface waves (i.e., averaged phase difference among multiple traces), FWI uses both phase and amplitude information of the whole observed data. Thus, FWI features higher resolution and better applicability to heterogeneous models. [Tran and Sperry \(2018\)](#) showed a relatively good agreement between near-surface structures estimated by FWI and MASW. However, there is no detailed comparison between the performances of MASW and FWI and, thus, little information on how to appropriately choose them to process shallow-seismic surface waves.

Table 1 A list of abbreviations used in this paper.

Abbreviations	Full names
FWI	Full Waveform Inversion
MASW	Multichannel Analysis of Surface Waves
CFWI	Classical FWI
MFWI	Multiscale FWI
EFWI	Envelope-based FWI
AFWI	Amplitude-spectrum-based FWI
STF	Source Time Function
FDM	Finite-Difference Method

In this paper, we compare MASW and FWI in reconstructing near-surface structures. We first illustrate the main steps in MASW and FWI, including classical FWI and three modified FWI approaches (MFWI, EFWI, and AFWI; a list of abbreviations used in this paper can be found in Table 1). We link these methods by discussing the subdata they use. We compare the ill-posedness and resolution of these methods by using a numerical example. We apply a sequential inversion strategy, in which MASW and FWI are performed successively, to two field data sets acquired in Olathe, Kansas, USA, and Rheinstetten, Germany, respectively. The inversion results are compared to borehole data and to a GPR profile, respectively, to verify the validity of the sequential-inversion strategy as well as to compare the performances of MASW and FWI in reconstructing near-surface structures.

2 MASW

In a layered model, surface-wave phase velocity V_{ph} is determined by a function D in a nonlinear, implicit form as

$$D(V_{ph}(f), \mathbf{m}) = 0, \quad (1)$$

where f represents frequency and \mathbf{m} represents the elastic model parameters (S-wave velocity, P-wave velocity, and density) as a function of depth (1D). We can calculate the surface-wave phase velocity by solving equation 1 numerically via means like the Thomson-Haskell method ([Thomson 1950](#); [Haskell 1953](#); [Ke et al 2011](#)), Knopoff method ([Knopoff 1964](#); [Schwab and Knopoff 1970](#)), reflection and transmission coefficients method ([Kennett 1974](#); [Chen 1993](#); [Pei et al 2008](#)), and delta-matrix method ([Watson 1970](#)).

In MASW we aim at minimizing the misfit between synthetic and observed dispersion curves (phase velocities over frequencies), which can be written as

$$\Phi_{MASW}(\mathbf{m}) = \frac{1}{2} \sum_f \|V_{ph}^{syn}(f) - V_{ph}^{obs}(f)\|^2 \quad (2)$$

where $V_{ph}^{syn}(f)$ and $V_{ph}^{obs}(f)$ are the synthetic and observed phase velocities, respectively. The misfit function may also be weighted upon a data covariance matrix ([Xia et al 2010](#)) or be stabilized by adding model constraint terms ([Xia et al 1999](#); [Piatti et al 2013](#)). However, we do not incorporate them here for the sake of brevity.

Two main steps involved in MASW are the extraction and the inversion of dispersion curves (Fig. 1). For the extraction of surface-wave dispersion curves we need to transform the wavefield data from the space-time (x - t) domain to the frequency-wavenumber (f - k) or the frequency-velocity (f - v) domain by a transform function T as in

$$U(f, v) = T[u^{obs}(x, t)] \quad (3)$$

where $U(f, v)$ represents the surface-wave spectrum in the f - v domain (or equivalently $U(f, k)$ in the f - k domain), which is also named dispersion image (Fig. 1); $u^{obs}(x, t)$ is the seismic wavefield observed by a multichannel system in the x - t domain (shot gather in Fig. 1). The transform function T can be implemented via means like phase shift ([Park et al 1998](#)), slant stacking ([Xia et al 2007](#)), generalized S-transform ([Askari](#)

and Hejazi 2015), and high-resolution linear Radon transform (Luo et al 2008). We pick the continuous dispersive-energy peaks over frequency in the spectrum $U(f, v)$ as surface-wave dispersion curve ($V_{ph}^{obs}(f)$ in equation 2). The spatial change in the dispersion curve, which could indicate the lateral variation of the model (Strobbia and Foti 2006; Vignoli and Cassiani 2010; Vignoli et al 2011), however, is neglected in each multichannel data set. In other words, we adopt a 1D approximation for the subsurface Earth structure below each multichannel spread used for dispersion analysis.

Due to the plane-wave (high-frequency) approximation (Aki and Richards 2002; Foti et al 2014), MASW may suffer from a near-field effect that surface waves have not yet fully developed into plane waves at short offsets, resulting in an underestimation of Rayleigh-wave phase velocities (Pan et al 2013b). We assume that a clear and continuous dispersive energy peak in the dispersion image represents an individual mode of surface waves. This assumption is valid in most of the cases. However, a visually continuous energy peak may shift from one mode to another at some frequencies. This phenomenon is called mode osculation (Boaga et al 2013) or mode kissing (Xia et al 2012), and has recently been observed in a real-world example (Gao et al 2016). Because it is almost impossible to identify the conversion between different modes in a continuous energy peak by using one dispersion image alone, it is recommended to use multi-component data (Ikeda et al 2014; Dal Moro et al 2015, 2018) or to jointly use Rayleigh and Love-wave data (Gao et al 2016) to reduce the possibility in the misidentification of surface-wave dispersion curves.

After picking a dispersion curve, we invert it to estimate the 1D Earth structure below the spread. Many algorithms have been proposed over the years to invert surface-wave dispersion curves, including both local search methods based on the gradient or Jacobian matrix (Fréchet derivative) (e.g., Xia et al 1999) and global search methods that solve the optimization problem stochastically (e.g., Yamanaka and Ishida 1996; Socco and Boiero 2008; Boaga et al 2011; Song et al 2012). By interpolating multiple 1D profiles estimated from different spreads using MASW, a pseudo-2D (Bohlen et al 2004; Luo et al 2009; Mi et al 2017) or 3D model (Boiero et al 2011; Strobbia et al 2011; Ikeda and Tsuji 2015; Pan et al 2016a, 2018b) can then be reconstructed. Since each picked dispersion curve represents a harmonic mean of the velocity structure below the spread (Boiero and Socco 2010), the lateral heterogeneity would be partly reconstructed if the lateral changes in the dispersion curves could be estimated accurately (Mi et al 2017). In other words, shorter spreads may provide us a higher resolution in the final pseudo model due to the 1D approximation. On the other hand, however, longer spreads improve the resolution of the dispersion image (Forbriger 2003) which is significant for the accuracy of a picked dispersion curve. Thus, there is a trade-off between accuracy and lateral resolution of MASW, and the final 2D or 3D model estimated by MASW is usually blurred. As we only use planar surface waves in MASW, the phase information related to some of the non-layered structures (e.g., scattered surface waves caused by lateral heterogeneity; Chai et al 2012; Bergamo and Socco 2014; Sloan et al 2015) is excluded after picking the dispersion curve since they do not behave as a dispersive continuous energy trend in the f - v domain. This is another reason for the difficulty to accurately reconstruct those non-layered structures using MASW.

3 FWI

3.1 Classical FWI

The relationship between the seismic wavefield u and an elastic model \mathbf{m} (1D, 2D, or 3D) can be written as

$$u(t) = G(\mathbf{m}) * S(t) \quad (4)$$

where $G(\mathbf{m})$ denotes the Green's function of a model \mathbf{m} , $S(t)$ denotes a seismic source time function (STF), and the symbol $*$ represents convolution in the time domain. Equation 4 can be simulated by solving the wave equation numerically. In this paper, we adopt a staggered-grid finite-difference method (FDM) as a forward solver to simulate 2D elastic (P-SV) waves (Virieux 1986).

FWI aims at minimizing the misfit between synthetic and observed waveforms. In classical FWI (CFWI), the L2-norm misfit function Φ_{CFWI} is defined as

$$\Phi_{CFWI}(\mathbf{m}) = \frac{1}{2} \sum_{s_r, x_r} \int_0^T \|u^{syn}(t, x_r; s_r) - u^{obs}(t, x_r; s_r)\|^2 dt \quad (5)$$

where u^{syn} and u^{obs} denote the synthetic and observed waveforms, respectively; s_r and x_r represent the sources and receivers, respectively, and T represents the total recording time. Although we could use different norms to define the objective function (Brossier et al 2010), here we use the L2-norm since it is the most widely-used objective function in both MASW and FWI.

Although attempts have been made in using global optimization algorithms to solve the inverse problem in FWI (Zeng et al 2011a; Aleardi et al 2016; Xing and Mazzotti 2018), most of the FWI studies use

gradient-based local optimization algorithms due to a huge number of parameters in \mathbf{m} . The huge number of parameters also makes the direct numerical calculation of the Jacobian matrix (Fréchet derivative) computationally expensive. The gradient of the FWI misfit function with respect to model parameters, however, can be calculated efficiently using an adjoint state algorithm (Plessix 2006), in which only two wavefield simulations are required: One simulation of the forward-propagating wavefield (state variable), and one simulation of the back-propagating residual wavefield (adjoint-state variable). The gradient can be calculated by correlating the state and the adjoint-state variables. By iteratively updating the model \mathbf{m} with a local optimization algorithm, we can finally obtain a physical model which can explain the observed waveform appropriately. Comparisons between performances of different optimization algorithms in FWI can be found in Métivier et al (2013), Métivier and Brossier (2016) and Liu et al (2017).

3.2 Modified FWI approaches

The classical FWI misfit function is affected by the existence of numerous local minima, which greatly increases the ill-posedness of the inverse problem. One efficient way to reduce the possibility of getting trapped in a local minimum is to adopt an appropriate initial model that is close to the true model. However, the creation of an appropriate initial model cannot always be guaranteed in real-world cases. Another way to mitigate the nonlinearity of FWI is to modify its objective function. Three approaches that have been proposed and applied to shallow-seismic data are the multiscale FWI (Bunks et al 1995; Groos et al 2017), the amplitude-spectra-based FWI (Pérez Solano et al 2014), and the envelope-based FWI (Bozdag et al 2011; Wu et al 2014; Yuan et al 2015; Borisov et al 2017).

In MFWI we start at inverting the low-frequency (long-wavelength) part of the data, and then progressively introduce high-frequency (short-wavelength) content in the data space. It can be expressed as

$$\Phi_{MFWI}(\mathbf{m}) = \frac{1}{2} \sum_{s_r, x_r} \int_0^T \|F[u^{syn}(t, x_r; s_r)] - F[u^{obs}(t, x_r; s_r)]\|^2 dt \quad (6)$$

where F represents a frequency filter. MFWI provides a natural framework to perform the scale separation of the data by using different frequency filters. It uses subdata which only contain the long-wavelength (low-frequency) components to reconstruct a general background model in the beginning stage, and then progressively includes the subdata of shorter wavelengths (higher frequencies) to reconstruct structures of smaller scales. MFWI becomes equivalent to CFWI when the frequency filter covers the whole range of interest.

In AFWI a new misfit function Φ_{AFWI} is defined as

$$\Phi_{AFWI}(\mathbf{m}) = \frac{1}{2} \sum_{s_r, w} \int_0^{f_{max}} \int_0^{k_{max}} \| |U_w^{syn}(f, k; s_r)| - |U_w^{obs}(f, k; s_r)| \|^2 df dk \quad (7)$$

where U_w^{syn} and U_w^{obs} represent the f - k spectra of the spatially windowed synthetic and observed data, respectively; w represents the spatial windows, and $|\cdot|$ represents the absolute value of a complex number. The data space of AFWI has been transformed from the x - t domain to the f - k domain, and AFWI tries to minimize the difference between the amplitude spectra of the observed and synthetic waveforms.

By defining the misfit associated with surface-wave dispersion spectra (U in equations 3 and 7), AFWI can be viewed as an intermediate way between MASW and the classical FWI. AFWI avoids the ambiguity caused by the picking of modal dispersion curves in MASW and also includes amplitude information of surface waves in the inversion. AFWI is similar to modified MASW approaches presented in Forbriger (2003) and Ryden and Park (2006), in which the inversion tries to minimize the difference between an observed phase-velocity spectrum and that simulated from a theoretical layered model. AFWI adopts a 2D forward solver while the modified MASW approaches are based on a 1D structure. Thus, AFWI is better applicable to laterally heterogeneous models than the modified MASW approaches.

In AFWI cycle skipping happens when the inversion tries to fit a single-mode surface-wave spectrum to another mode, and is equivalent to a mode misidentification of surface waves in MASW (Zhang and Chan 2003). So the wider the surface-wave energy trend is (equivalently, the lower the resolution in the wavenumber domain is), the lower the possibility that AFWI gets trapped in a local minimum. Since the resolution of a surface-wave energy trend in the wavenumber domain is inversely proportional to the length of the spread (Forbriger 2003), AFWI is able to balance the resolution of the f - k spectra to avoid cycle skipping by incorporating spatial windows of different lengths (Pérez Solano et al 2014).

In EFWI, the misfit function Φ_{EFWI} is defined as

$$\Phi_{EFWI}(\mathbf{m}) = \frac{1}{2} \sum_{s_r, x_r} \int_0^T \| [E^{syn}(t, x_r; s_r)]^p - [E^{obs}(t, x_r; s_r)]^p \|^2 dt \quad (8)$$

where E^{syn} and E^{obs} are the envelopes of synthetic and observed waveforms, respectively; p is the power for the envelope data. The envelope function E can be obtained via Hilbert transform as

$$E(t, x_r; s_r) = \sqrt{u^2(t, x_r; s_r) + H^2[u(t, x_r; s_r)]} \quad (9)$$

with H denoting the Hilbert transform.

Similar to MFWI, EFWI also uses the long-wavelength part of the data in the first stage. However, it performs a nonlinear scale separation by an envelope operator and, thus, has the ability to extract ultra-low-frequency signals (Wu et al 2014).

Overall, MFWI, AFWI, and EFWI are different hierarchical strategies for FWI. All of them firstly invert a part of the data (subdata) that is less sensitive to cycle skipping. By choosing appropriate frequency filters (F in equation 6), spatial windows (w in equation 7), and numbers of power (p in equation 8), MFWI, AFWI, and EFWI are able to separate the data into different scales, so that each modified FWI approach provides a multi-stage hierarchical FWI strategy. These three approaches share the same adjoint-state equation with CFWI. In other words, the only difference in their gradient calculation exists in their corresponding adjoint sources, which is related to their objective functions. By incorporating spatial windows, however, AFWI has a higher computational cost compared to the others because the misfit gradient needs to be calculated for each window. CFWI, though named as 'classical', is rarely used nowadays due to its high nonlinearity, while the modified approaches are more widely used in order to address the nonlinearity. We will show these features in the following numerical examples.

4 NUMERICAL EXAMPLES

Table 2 A simple model for numerical testing.

	S-wave velocity (m/s)	P-wave velocity (m/s)	density (g/cm ³)	thickness (m)
Layer 1	200	500	2.0	6
Half space	400	1000	2.0	∞

A layered model (Table 2) is used to compare the performances of MASW and FWI (including both the classical and the three modified FWI approaches) in reconstructing near-surface structures. The observed and synthetic waveforms for FWI are simulated by FDM. A 25 Hz Ricker wavelet with 50 ms delay is used as STF and is generated as a vertical force. Forty-eight two-component receivers are placed along the free surface with a nearest offset of 4 m and a trace interval of 1 m and record both vertical and horizontal components (an observed vertical-component shot gather is shown in Fig. 2a). We use both vertical and horizontal components in the numerical example since multicomponent data outperform single-component data in shallow-seismic FWI (Masoni et al 2013a,b; Nuber et al 2017). The observed (Fig. 2b) and synthetic input data for MASW is the fundamental-mode dispersion curve from 10 to 80 Hz with a sampling interval of 2 Hz, which is calculated via the Thomson-Haskell method (Haskell 1953).

Since surface waves are much more sensitive to the S-wave velocity compared to the P-wave velocity and density in both MASW and FWI (Xia et al 1999; Groos et al 2017), we only test the influence of the S-wave velocity (V_s) on the objective functions of MASW and FWI. The V_s model consists of two values: a top-layer velocity V_{s_top} , which ranges from 100 to 300 m/s, and a homogeneous half-space (bedrock) velocity $V_{s_bedrock}$ that ranges from 300 to 500 m/s. We use the true P-wave velocity and density models as well as the true thickness of the first layer (Table 2) in all synthetic tests.

4.1 Forward modeling test

The objective functions of CFWI and MASW calculated with equations 2 and 5 are shown in Fig. 3. The global minimum region is quite narrow in the CFWI objective function (area in blue color in Fig. 3a). Most of the negative gradients in the objective functions (arrows in Fig. 3) are pointing parallel to the V_{s_top} axis. It indicates that CFWI is most sensitive to the velocity of the top layer. In the regions where V_{s_top} is more than 10 % off its true value ($V_{s_top} > 220$ m/s or $V_{s_top} < 180$ m/s), negative gradient directions mostly point away from the global minimum (center point of each image in Fig. 3). Consequently, CFWI may not find the true model if the initial velocity of the top layer differed more than 10% from the true value. It shows a strong restriction on the accuracy of the initial model. Furthermore, the gradient directions change irregularly in the model space, indicating a fairly high nonlinearity of CFWI. The narrow region

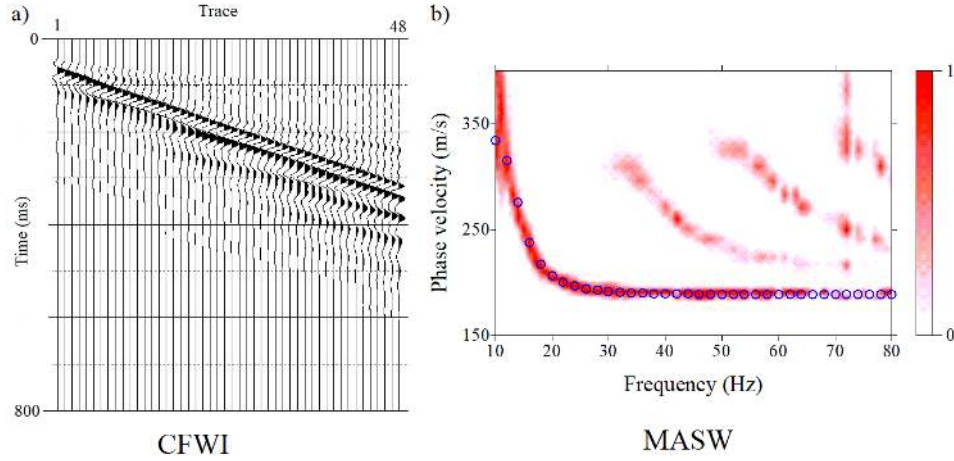


Fig. 2 a) Observed vertical-component shot gather in CFWI. The observed data are dominated by Rayleigh waves. b) Dispersion image in MASW obtained from the vertical-component shot gather. The observed phase velocities (circles) are calculated theoretically by using the true model. They nicely match the energy peak in the dispersion image.

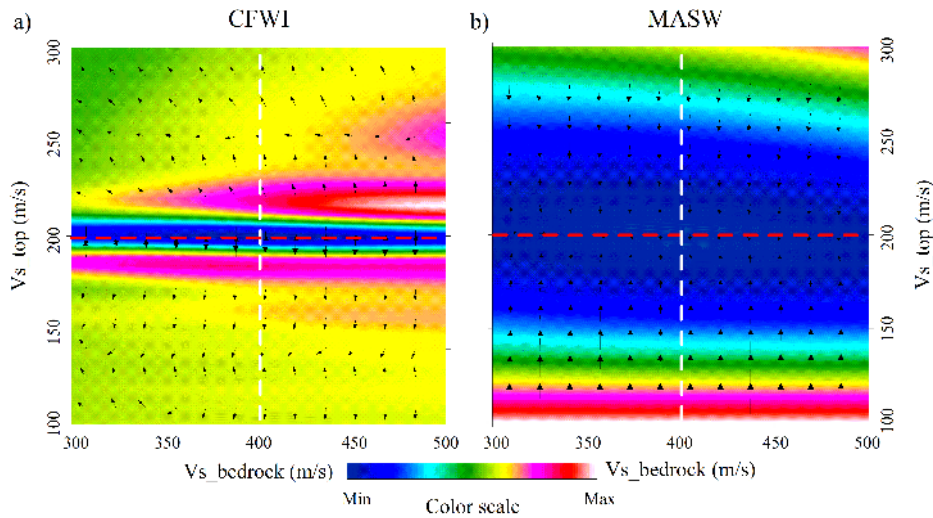


Fig. 3 Objective functions of a) classical FWI and b) MASW in the numerical test. Color represents the value of the objective function. Arrows represent the negative gradient of the objective function at that location, and their length depends on the absolute value of the gradient. Red and white dashed lines represent the locations of the true top-layer and bedrock velocities (Table 2), respectively.

of the global minimum in CFWI, however, indicates a good resolution of the reconstructed model and fast convergence if the initial model is accurate enough.

The MASW objective function (Fig. 3b) is much smoother. It shows a wide range of the global minimum basin that is around 8 times its width in CFWI. All negative gradient directions point towards the correct top-layer velocity, indicating a fairly small dependence of MASW on the initial model compared to CFWI. The negative gradient directions change slowly and smoothly in the model space, indicating, on one hand, high robustness against the initial model but, on the other hand, a slow convergence.

Similarly, we calculate the objective functions of the modified FWI approaches by using a high-cut filter of 10 Hz in MFWI, a spatial window with a length of the whole spread (48 traces) in AFWI, and $p = 1$ in EFWI (Fig. 4). The wavelengths of the observed waveforms in MFWI and EFWI are much longer than those in CFWI (Figs. 2 and 4), which reduces the possibility of cycle skipping. The global minima (Fig. 5) are much broader in the cases of MFWI, AFWI, and EFWI compared to CFWI but narrower compared to MASW. Most of the negative gradients in the modified FWI approaches point smoothly towards the global minimum. The nonlinearity of CFWI can be reduced by modifying its objective function. In this example, EFWI (Fig. 5c) has the widest global minimum region and the lowest nonlinearity among the FWI approaches. It is worthwhile to mention that by incorporating a shorter spatial window, AFWI is able

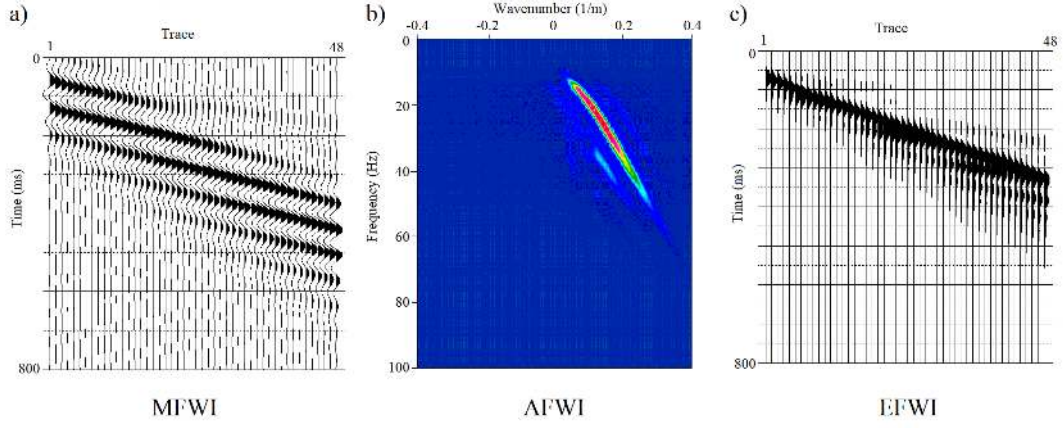


Fig. 4 Input data for a) multiscale FWI, b) amplitude-spectra-based FWI, and c) envelope-based FWI in the synthetic test.

to further reduce its nonlinearity. However, it comes at the cost of increased computational effort in the calculation of the gradient.

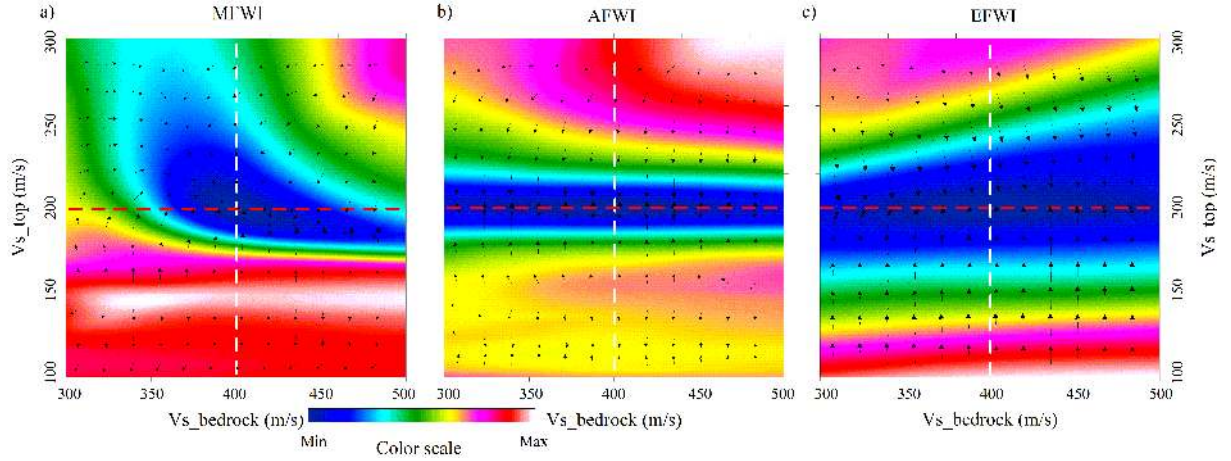


Fig. 5 Objective functions of a) multiscale FWI, b) amplitude-spectra-based FWI, and c) envelope-based FWI in the numerical test. Color and arrows have the same meaning as explained in Fig. 3.

4.2 Inversion test

We perform a series of two-parameter inversion tests on each method to compare their dependence on the initial model. The same model (Table 2) and data (Figs. 2 and 4) presented above are used, and we only invert for the two-parameter Vs model. The model space is the same as in the previous example (V_{s_top} ranges from 100 to 300 m/s, and $V_{s_bedrock}$ ranges from 300 to 500 m/s). We adopt a conjugate-gradient (CG) method (Hestenes and Stiefel 1952; Gilbert and Nocedal 1992) as the optimization algorithm. The gradient of the objective function is calculated by a finite-difference approximation (Nocedal and Wright 2006) in which a small perturbation is added to the two model parameters (V_{s_top} and $V_{s_bedrock}$), respectively.

Fig. 6 shows the solution paths in MASW and EFWI when an initial model with $V_{s_top} = 104$ m/s and $V_{s_bedrock} = 304$ m/s is chosen (starting point in Fig. 6). Both MASW and EFWI successively find the global minimum. Both solution paths show that the first few iterations mainly focus on the updates in V_{s_top} , while updates in $V_{s_bedrock}$ are mainly done when V_{s_top} is very close to its true value. When using the same initial model in the other cases (CFWI, AFWI, MFWI), however, the solution path goes out of the model space, which is regarded as a divergence in the inverse problem.

After performing inversion tests on all initial models in the model space, 96% of the models can successfully converge to the global minimum in MASW (red asterisks in Fig. 7a). The 'divergent' points (starting

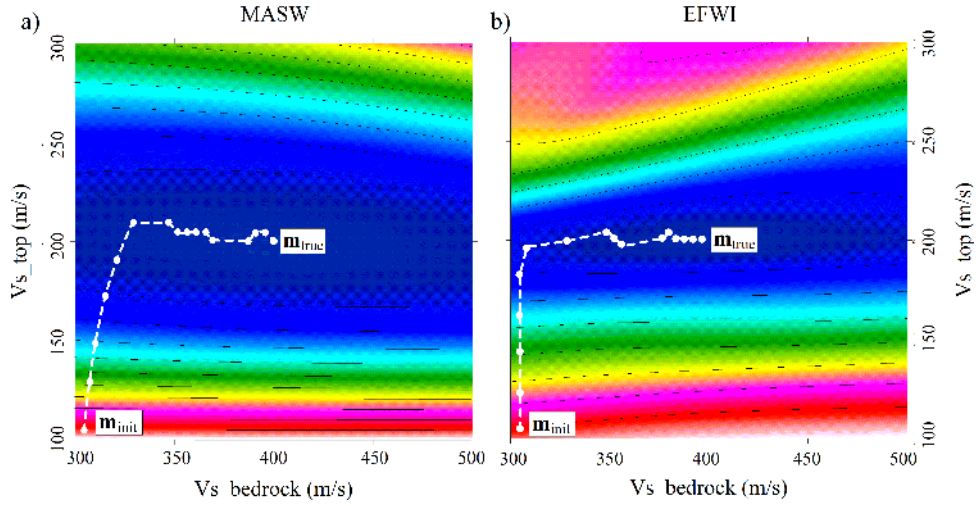


Fig. 6 Examples of solution paths for a) MASW and b) EFWI in the two-parameter inversion examples. Dashed lines and dots are the solution paths and iterative solutions, respectively. The starting point (initial model) in these two examples is $V_{s_top} = 104$ m/s and $V_{s_bedrock} = 304$ m/s.

models which fail to converge to the global minimum; blue asterisks in Fig. 7a) are mainly located at the boundaries of the model space. Some of them are treated as 'divergent' because our model space is not big enough to search for their solution paths which may finally lead towards the global minimum. In other words, some of the 'divergent' points located at the boundaries of the model space may become 'convergent' if we expand our model space. Overall, this inversion test shows a relatively low dependence of MASW on the initial model.

Similarly, we can find the global minimum by using 17%, 72%, 65%, and 94% of the initial models in CFWI, MFWI, AFWI, and EFWI (red asterisks in Fig. 7b-e), respectively. In CFWI, most of the 'convergent' points are located in a region where V_{s_top} is less than 10% off its true value, and only 17% of the starting points in the model space are able to converge to the global minimum. This agrees with our discussion in the forward modeling test, and again shows a high dependence of CFWI on the initial model. This dependence on the initial model is greatly reduced when a modified approach is adopted. In the cases of MFWI and AFWI, more 'convergent' points are located in a region where V_{s_top} is higher than its true value compared to the other side. This is because these methods primarily use the kinematic information (traveltime) of the data, which is reciprocal to the velocity value. Thus, a higher velocity has less influence on the kinematic information of the data compared to a lower velocity. This behavior provides a useful suggestion when preparing an initial model for these methods. Although the sensitivity of all objective functions is quite weak towards $V_{s_bedrock}$, we are still able to reconstruct $V_{s_bedrock}$ even if the initial $V_{s_bedrock}$ is relatively far off its true value. This is because all these synthetic tests were performed on noise-free data, which enables us to use even weak signal present in the data. We may not be able to accurately reconstruct $V_{s_bedrock}$ if the data are noise-contaminated. Overall, these inversion tests prove that the success of CFWI is highly dependent on the initial model, while this dependence decreases when adopting a modified FWI approach. MASW has a lower dependence on the initial model, which can be exploited to provide an appropriate initial model for FWI.

4.3 Resolution test

A checkerboard model is used to compare the resolution of MASW and FWI. A homogeneous half-space model with an S-wave velocity of 200 m/s, a P-wave velocity of 500 m/s, and a density of 2000 kg/m³ is used as the background model. The checkerboard is formed by blocks of 1 m × 1 m, and the S-wave velocity of each block is 220 or 180 m/s depending on its position (Fig. 8), i.e., $\pm 10\%$ perturbation in S-wave velocity is added to the background model. Twenty-four two-component geophones are placed along the free surface with an interval of 1 m (red dashed line in Fig. 8a). Six shot gathers are simulated with a vertical-force source spaced every 6 m (red stars in Fig. 8a). The nearest source-receiver offset for the leftmost source is 3 m. A shifted Ricker wavelet with a center frequency of 40 Hz is used as the STF. The minimal wavelength of the observed surface wave is around 2 m, which is twice the size of the checkerboard block.

We use the background model as the initial model and apply CFWI on the observed data. The true STF is used and only the S-wave velocity model is updated during the inversion. The same CG algorithm as before

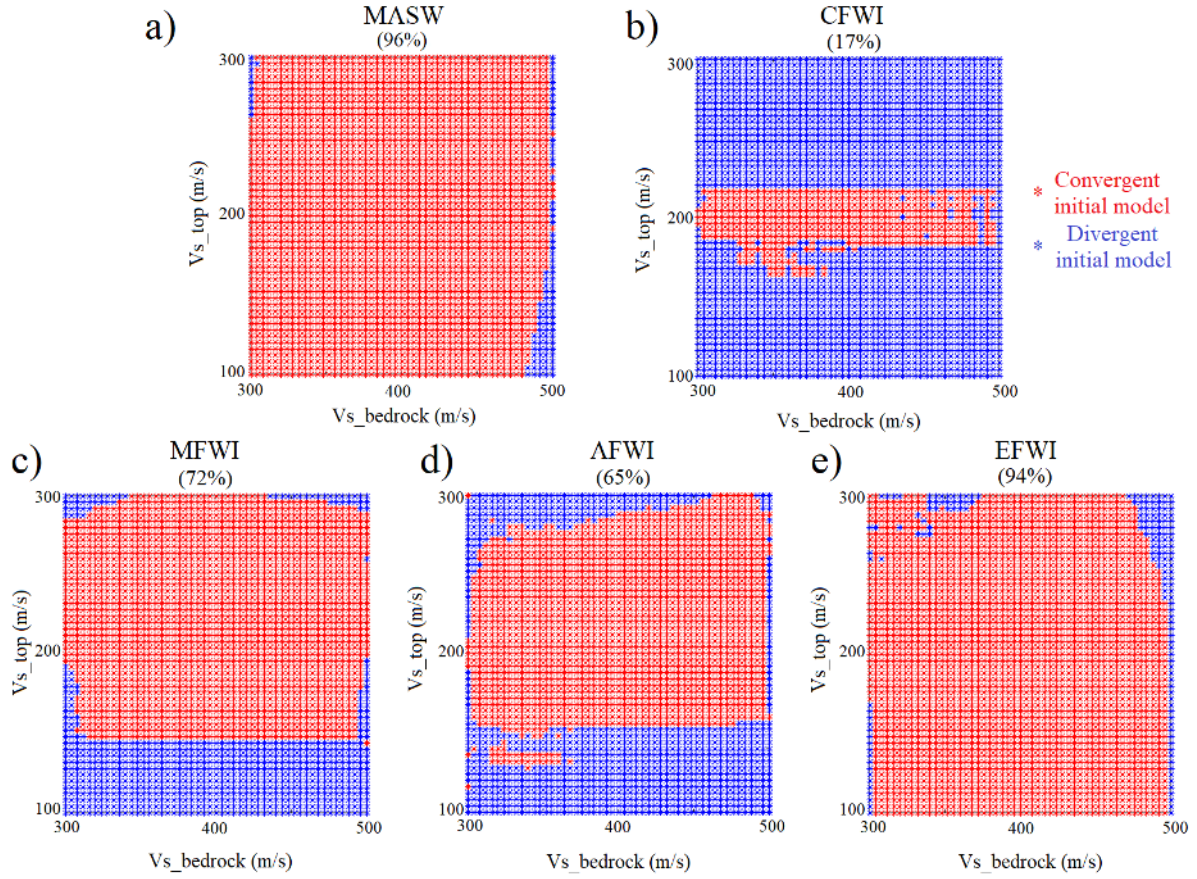


Fig. 7 Distribution of convergent and divergent initial models of a) MASW, b) CFWI, c) MFWI, d) AFWI, and e) EFWI in the two-parameter inversion examples. Red and blue asterisks are the starting points (initial models) which converge to and diverge from the global minimum, respectively. The global minimum is located at the center of the model space ($Vs_{top} = 200$ m/s and $Vs_{bedrock} = 400$ m/s).

is used as the optimization algorithm, and the gradient is calculated by the adjoint state algorithm (Plessix 2006). The checkerboard model can be reconstructed using CFWI (Fig. 8b), which proves a relatively high resolution (approximately half a wavelength). The lower left and right corners in the checkerboard are not reconstructed as well as the other areas, mainly due to a lower illumination in the lower corners. Similarly, we perform MFWI (by applying a low-pass filter with its upper frequency limit progressively increasing from 20 to 40, 60, 80 and 100 Hz), AFWI and EFWI on the checkerboard model (Fig. 8c-e). All the modified FWI approaches successfully reconstruct the checkerboard, indicating all FWI approaches have a spatial resolution of half a wavelength. The checkerboard is more smeared in the result of EFWI compared to the other results, showing that the resolution of EFWI is lower than the other methods.

We also estimate the dispersion image of the simulated shot gather generated by the leftmost source (Fig. 9a) in the true model. Due to the near-field effect, the Rayleigh wave is not fully developed in the low-frequency range (i.e., frequency lower than 20 Hz). The energy trend in the dispersion image is almost non-dispersive, which indicates that the model is relatively homogeneous. We also estimate the dispersion image of a synthetic shot gather simulated by the same source but with the homogeneous background model (synthetic data corresponding to the initial model in CFWI; Fig. 9b). The two dispersion images look very similar to each other. Two dispersion curves are automatically picked along the energy peak from these two dispersion images (circles and triangles in Fig. 9a and b, respectively). The two picked dispersion curves are very close to each other, with a maximal difference of only 1 m/s at each discrete frequency point (Fig. 9c). It shows that the dispersion image is not sensitive to the existence of the checkerboard. In other words, we are not able to reconstruct the checkerboard model by using MASW due to its low resolution. Similar behavior is observed for the shot gathers generated by the other sources. This numerical example shows that FWI has a much higher resolution as well as applicability for laterally heterogeneous models, while MASW is not able to reconstruct lateral heterogeneity of small scale.

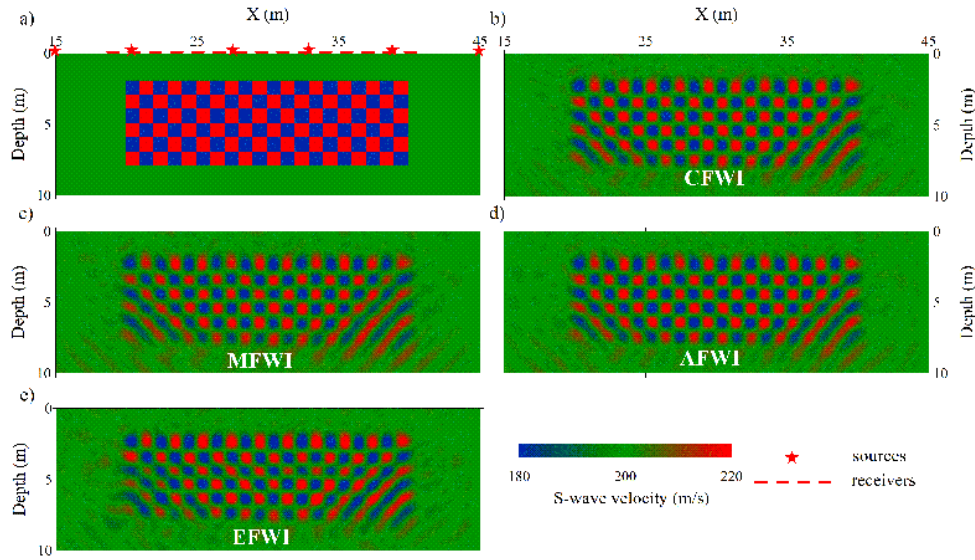


Fig. 8 Checkerboard model test. a) True model. Stars represent the locations of the sources, and the dashed line represents the geophone spread. b), c), d) and e) are the inversion results of CFWI, MFWI, AFWI and EFWI, respectively. A homogeneous background model is used as the initial model in all tests.

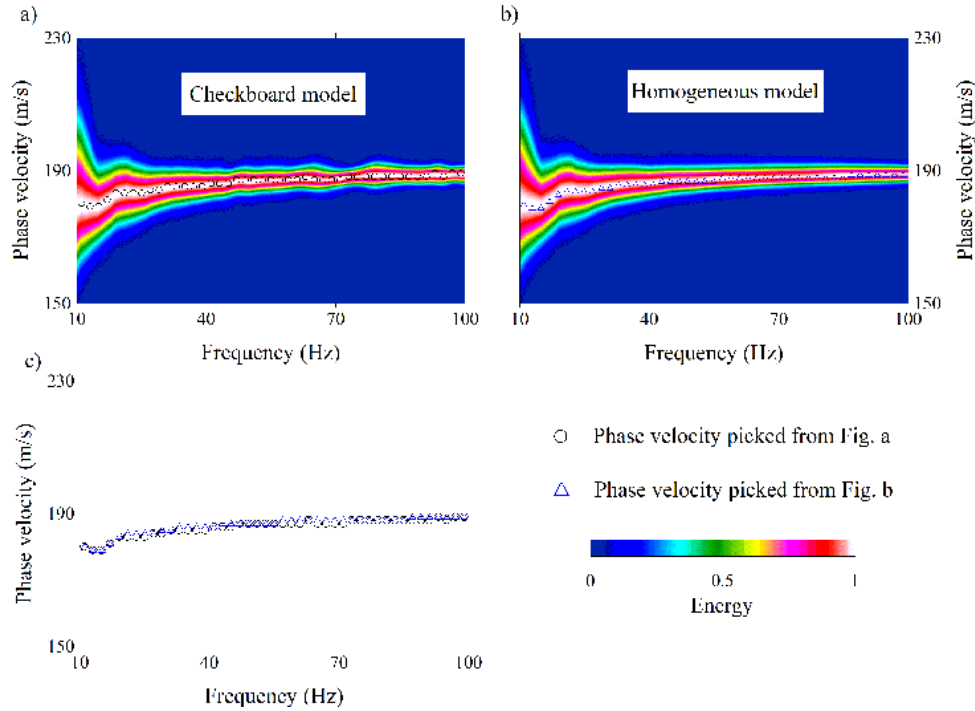


Fig. 9 Dispersion image estimated from the shot gathers generated by the leftmost source. a) and b) represent the dispersion images corresponding to the checkerboard (true) model and homogeneous (initial) model, respectively. Circles and triangles are the phase velocities picked along the energy peak in a) and b), respectively. c) Comparison of the dispersion curves picked from a) and b). The maximal difference between the two phase velocities at each frequency is only 1 m/s.

4.4 Hierarchical way from MASW to FWI

From the numerical examples above, it can be seen that CFWI possesses both high nonlinearity and high resolution at the same time, and its success is highly dependent on the adoption of an appropriate initial model. On the other hand, MASW shows a relatively low dependence on the initial model, as well as a low resolution. The nonlinearity and resolution of all the modified FWI approaches are between that of CFWI and MASW, implying a trade-off effect between the resolution and nonlinearity in the inverse problem. It suggests that sequential applications of MASW, modified FWI approaches, and CFWI to shallow-seismic data can provide a hierarchical way to delineate near-surface structures, which progressively proceeds from

low to high in both the resolution and the nonlinearity. Although according to the numerical example EFWI has the lowest nonlinearity among the three approaches, and AFWI has a similar nonlinearity compared to MFWI, these features do not always hold, especially if the model or the scale parameters (frequency band in MFWI, spatial window in AFWI, and power of the envelope of waveforms in EFWI) are changed. As each modified FWI approach has its own way to perform scale separation on the data, we can usually find some appropriate scale parameters to make those methods equivalent regarding their level of nonlinearity. So it is more advisable to iterate more scales in one modified FWI approach, rather than adopting more approaches but with insufficient scales or iterations in each approach. It should be noted that we only have two variables in the numerical test, and the ill-posedness of the inverse problem will increase with the inclusion of more variables (e.g., a greater number of unknowns in Vs or the inclusion of Vp and density in the inverse problem).

Although each modified FWI approach could provide a complete strategy for scale separation, each of them has some unique characteristics. For example, EFWI has the highest ability in recovering long-wavelength components among the three approaches; AFWI has the lowest sensitivity to random noise since random noise is usually uncorrelated in the f - k domain; MFWI provides the smoothest transition towards CFWI and, thus, it may have higher resolution than the other two approaches. These characteristics make the selection data-oriented or target-oriented. In the following real-world cases, we adopt MFWI as the modified approach. This is because the sensitivity scale of a surface wave mainly depends on its wavelength (frequency); thus, MFWI can provide a more efficient way to focus on the scale of subdata which are most sensitive to our geological targets (e.g., bedrock or shallow trench). This advantage is also shown in Fig. 4 in which the gradients are more inclined to the horizontal direction (bedrock velocity) in MFWI compared to the other two approaches, indicating that MFWI is more sensitive to the deep part (bedrock velocity) in a low-frequency scale. MFWI becomes equivalent to CFWI in the last stage since there we include the whole frequency range of interest.

5 FIELD EXAMPLES

5.1 An example in Olathe, USA

A field data set was acquired at Olathe, Kansas, USA in the 1990s to map the shape of the bedrock (Miller et al 1999). We used a subset of the acquired data to test the performances of MASW and FWI in reconstructing the near-surface structure. A vertical source and forty-five vertical-component geophones were placed along the survey line, with the nearest offset of 3.6 m and a trace interval of 0.6 m (refer to Fig. 16). A roll-along manner was used during data acquisition, and the whole spread was moved 1.2 m (2 traces) towards the eastern direction (end of spread) with each new shot. A total of ten shot gathers are used in our example.

We obtained a Rayleigh-wave dispersion image via high-resolution linear Radon transform (Luo et al 2008) using the middle (6th) shot gather (Fig. 10). A dispersive Rayleigh-wave energy trend can clearly be identified in the f - v domain. We manually picked along the peaks of the energy trend as Rayleigh-wave dispersion curve (circles in Fig. 10) and inverted it by using a least-squares algorithm (Xia et al 1999). The density model which gradually increases from 1800 kg/m³ to 2150 kg/m³ with depth was not updated during the inversion due to its low sensitivity (Xia et al 1999). We did not pick any Rayleigh-wave phase velocity below 30 Hz because the dispersive energy changes abruptly at 30 Hz, which indicates that the dispersive energy below 30 Hz may not belong to the fundamental-mode Rayleigh wave (Gao et al 2014). An eight-layer model in which the thicknesses of layers gradually increase with depth was used in the inversion. No limitation was applied to the range of S-wave velocities. The 1D S-wave velocity profile (blue line in Fig. 11) suggests that the geotechnical bedrock (soft rock with an S-wave velocity higher than 360 m/s) is around 2 to 7 m in depth. Since the longest wavelength in our picked dispersion curve is only 10 m, the S-wave velocities below 5 m are less reliable compared to the part above 5 m. We also imaged the dispersion curves from the other shot gathers. However, the dispersion curves estimated from different shot gathers look very similar to each other. Thus, we did not perform the 1D MASW to multiple shot gathers to obtain a pseudo-2D S-wave velocity model. Since layer interfaces were predefined in MASW and may contain some errors, we smoothed the 1D result (dashed red line in Fig. 11) and extended it to a laterally homogeneous 2D model, and subsequently used it as initial S-wave velocity model for FWI. We also picked the first arrivals from all shot gathers and inverted their traveltimes to obtain a 1D P-wave velocity profile (black line in Fig. 11). It is obvious that the S-wave velocity model is not simply a scaled and smoothed version of the P-wave velocity model. Since the success of FWI highly depends on the adoption of an appropriate initial model while surface waves are most sensitive to S-wave velocity among all the elastic parameters, it is superior to use MASW to build an initial S-wave velocity model instead of deriving an initial S-wave velocity model by scaling and smoothing the P-wave velocity model obtained from traveltimes. Similarly,

we also smoothed (dotted red line in Fig. 11) and extended it to 2D for use as the initial P-wave velocity model in FWI. A homogeneous half-space density model with a value of 2100 kg/m^3 was used as the initial density model for FWI.

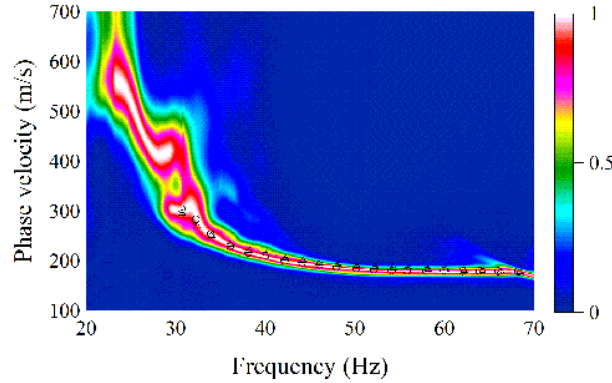


Fig. 10 Dispersion image obtained from the 6th raw shot gather via high-resolution linear Radon transform. Circles and triangles represent picked and inverted dispersion curves, respectively. Color represents the relative energy of the Rayleigh wave.

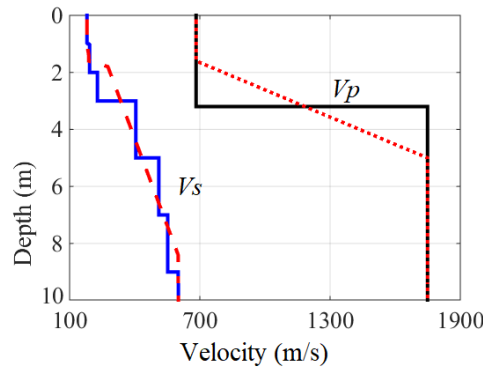


Fig. 11 Estimated 1D velocity models. The solid blue line represents the 1D S-wave velocity inversion result of MASW (Fig. 10). The solid black line represents the 1D P-wave velocity inverted from traveltimes of the first arrivals. Dashed and dotted red lines represent smoothed 1D S- and P-wave velocity models, respectively, that are extended and used as initial models for FWI.

We adopted a virtual-real source (VRS) method (Behura and Snieder 2013; Gao and Pan 2018) to extract the STF of all the sources (Fig. 12). Based on seismic interferometry, the VRS method does not require any prior information about the model and provides a model-independent way to estimate the STF. Ten STF's estimated by the VRS method show high similarity among each other, indicating that the estimated STF is fairly reliable. The STF's are not updated during the inversion due to their relatively high accuracy (Gao and Pan 2018). We applied a 3D-to-2D transformation to the observed data to correct errors in the phase and the amplitudes caused by a 2D forward solver (Forbriger et al 2014), and muted the noises arriving earlier than the first arrivals.

An FDM with a grid spacing of 0.2 m and a time step of 0.05 ms was used as the forward solver. The size of the whole model is 70 m in width and 30 m in depth (the half space in the estimated 1D model is extended to a depth of 30 m), and a 10 m thick multiaxial perfectly matched layer (Zeng et al 2011b) was applied to the left, right and bottom parts of the model. We updated the S- and P-wave velocity models during the inversion and kept the density model fixed. Because Rayleigh wave is more sensitive to S-wave velocity compared to P-wave velocity and density, we only interpret the S-wave velocity model in the real-world examples. A preconditioning semicircular taper was applied to the model gradient at each source position (Groos et al 2017), and the gradient was smoothed with a $1 \text{ m} \times 1 \text{ m}$ spatial Gaussian filter. The FWI was run on a computer with a four-core CPU of 3.7 GHz and 16 Gb RAM. Each iteration with a total of ten shot gathers took approximately 14 minutes, which is computationally affordable. This computational

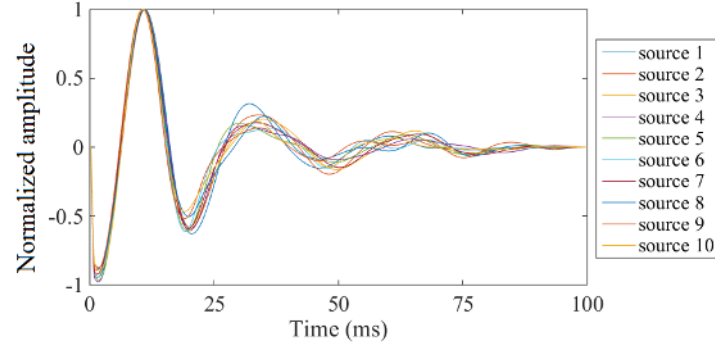


Fig. 12 Source time functions of the ten sources estimated from the VRS method.

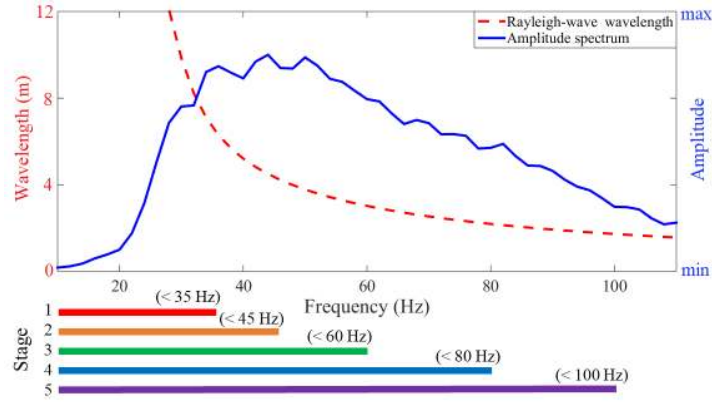


Fig. 13 Averaged frequency spectrum (blue line) of the ten shot gathers. The red dashed line denotes the corresponding Rayleigh-wave wavelength calculated from the picked dispersion curve in Fig. 10. Red, orange, green, blue and purple bars represent the frequency content that was used in different stages of MFWI.

cost is much lower compared to FWI on explorational or global scale due to a relatively small model in shallow seismics. However, FWI is still much more time-consuming compared to MASW, in which the whole inversion of one dispersion curve took less than a minute on the same computer.

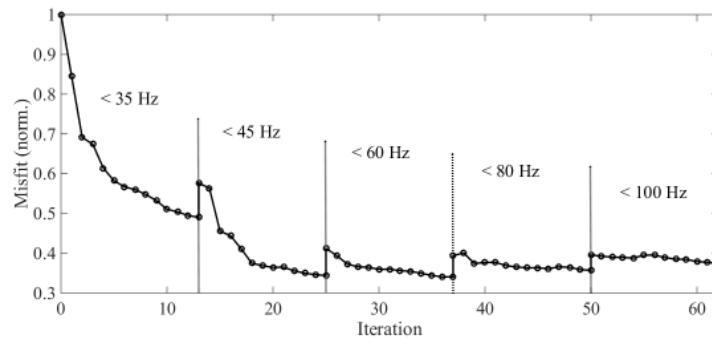


Fig. 14 Change of misfit value in MFWI of the field data acquired at Olathe, USA. Frequency range at each stage is marked in the figure.

We started MFWI by inverting a subset of data up to 35 Hz. The upper frequency limit of the low-pass filter is progressively increased to 45, 60, 80, and 100 Hz (bars in Fig. 13). The shortest corresponding wavelengths for these frequencies are 7.2, 4.2, 3.0, 2.2, and 1.8 m, respectively (red dashed line in Fig. 13). In other words, we started our inversion with long-wavelength surface waves (wavelength > 7.2 m), and progressively included surface waves of shorter wavelengths. We stopped our inversion at 100 Hz because our main interest is to delineate the shape of the bedrock, which has almost no influence on the high-frequency components ($f > 100$ Hz). The same CG algorithm used in the synthetic example was adopted here as the

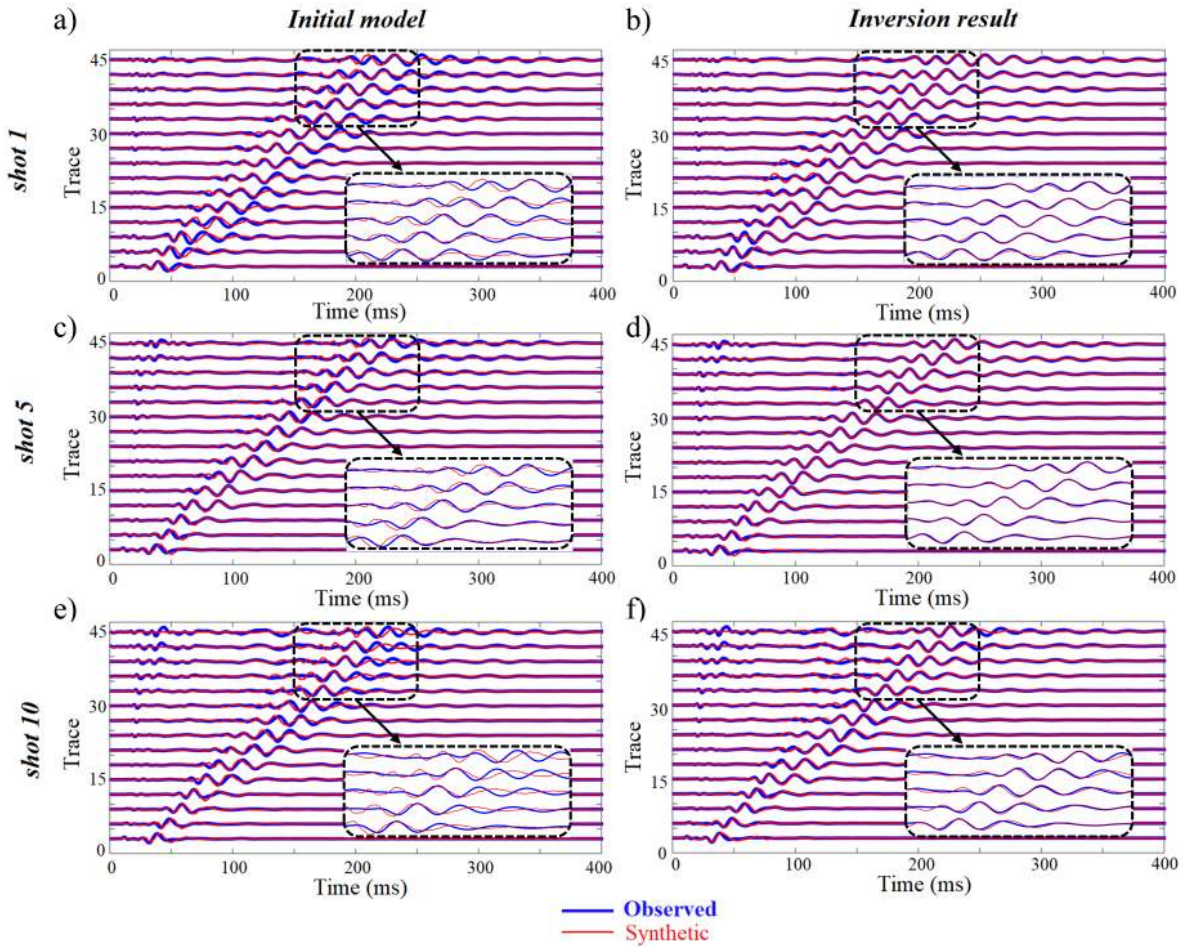


Fig. 15 Comparison between observed (blue) and synthetic (red) waveforms of the initial model (left) and inversion result of MFWI (right). The three rows denote the comparison of the 1st (top), 5th (middle), and 10th (bottom) shot gather. Blue and red lines represent observed and synthetic waveforms of every third trace, respectively. Dashed rectangular windows show the zoomed waveforms acquired at the last 15 traces in time between 150 ms and 250 ms.

optimization algorithm. An approximate inverse of the Hessian matrix by using its diagonal term (Plessix and Mulder 2004) was applied to precondition the gradient. A minimum of 11 iterations was performed at each stage, while the inversion moved to the next stage once the improvement in the misfit value became less than 1 %. The misfit values decreased fast in the first few iterations at each stage, and then the decrease gradually slowed down (Fig. 14). Finally, the misfit function converged after a total of 62 iterations.

Fig. 15 shows the comparison of observed and synthetic waveforms for the first, the fifth, and the last shot gather. The synthetic Rayleigh waves in the initial model fit the observed data quite well (left column in Fig. 15), implying a fairly high accuracy of the initial model estimated by MASW as well as the STF's estimated by VRS. Differences between the observed and synthetic waveforms of the initial model mainly exist in the far-offset traces, which is mainly caused by the missing information about lateral heterogeneity. The synthetic data of the inversion result nicely fits the observed waveforms (right column in Fig. 15), especially in the far-offset traces, indicating that a successful inversion has been achieved.

The MFWI result has a higher resolution compared to the initial model estimated by MASW, especially for the shape of the bedrock (dashed line in Fig. 16). The inversion result shows that the bedrock ranges from 2 to 6 m in depth, which agrees with borehole data (Miller et al 1999). Besides the shape of the bedrock, the result also shows the lateral change of the top layer. A borehole drilled at the eastern part of the survey line shows that the bedrock at that position is 4.2 m deep (Miller et al 1999), which nicely agrees with our inversion result (Fig. 16). It proves relatively high reliability and accuracy of the inversion result obtained by sequentially applying MASW and FWI to the observed shallow-seismic data.

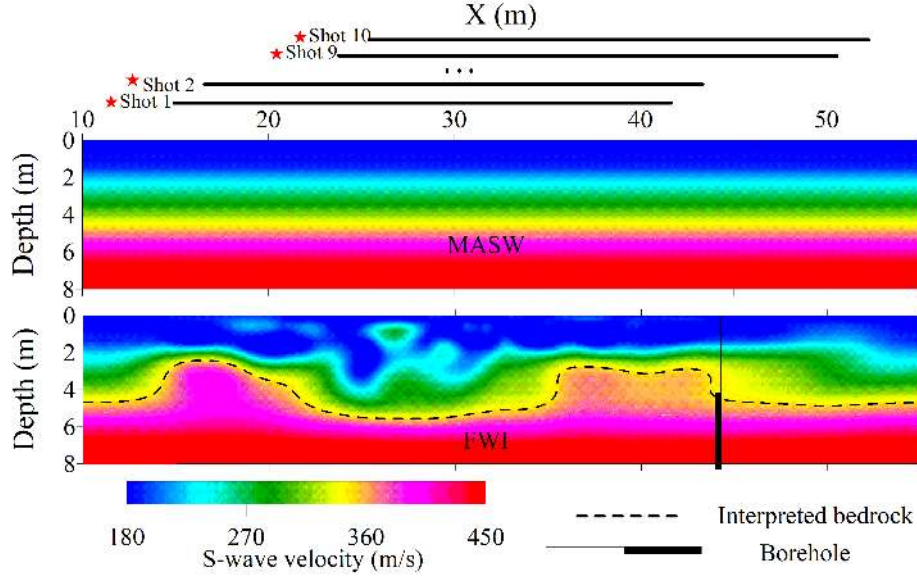


Fig. 16 S-wave velocity model for the Olathe data. Upper and lower images represent the smoothed initial model estimated by MASW and the MFWI inversion result after 62 iterations. Asterisks represent the locations of the ten sources. Solid lines represent locations of the ten geophone spreads.

5.2 An example in Rheinstetten, Germany

The second field data set was acquired in Rheinstetten, Germany. The near-surface material at the test site was mainly composed of layered fluvial sediments. A vertical source and forty-eight vertical-component geophones were placed along the survey line. The geophone spacing was 1 m (triangles in Fig. 17a). The source was placed every 4 m, and the first source position was located between the first and the second geophones. A total of 12 shot gathers are used in this example (asterisks in Fig. 17a).

Similarly, we built a 1D depth-dependent S-wave velocity model as the initial model for FWI by using MASW (Fig. 17a). The initial P-wave velocity was built by inverting traveltimes of the first arrivals. We applied the same 3D-to-2D transformation to the observed data as before. We delayed the whole shot gathers by 0.03 s to stabilize the STF inversion and killed the traces with a source-receiver offset shorter than 2 m since the signals in those traces are partly clipped (Gao and Pan 2016). Since the acquired data contain relatively strong attenuation effects, we used constant Q models ($Q_s=Q_p=15$; Bohlen 2002) as passive information with a viscoelastic forward solver, and performed STF inversion in the FWI to mitigate the influence of viscosity. The STF inversion could increase the ambiguity of the FWI result, although it efficiently decreased the misfit value because the differences in the waveforms caused by different models are partly projected into the STF inversion (Groos et al 2014, 2017). We started MFWI by inverting a subset of data up to 10 Hz. The upper frequency limit of the low-pass filter was progressively increased to 60 Hz with a 5 Hz interval, with a minimum of 3 iterations in each stage. The MFWI converged after a total of 52 iterations.

The inverted S-wave velocity model shows some 2D lateral variations of the subsurface (Fig. 17b). A "V"-shaped low-velocity body can be identified at the central shallow part of the model, which corresponds to a refilled trench at the test site. The inversion result also shows a velocity inversion (high-velocity layer on top of a low-velocity layer) around 50 m and 0.2 m depth. It is worth mentioning that a low-velocity body is also identified at the same location in the reconstructed P-wave velocity model; however, its "V" shape is less clear in the P-wave velocity model compared to the S-wave velocity model.

Fig. 18 shows the comparison of observed and synthetic waveforms of the first, the sixth, and the last shot gather. The synthetic waveforms in the initial model could not fit the observed data (left column in Fig. 18), which is mainly caused by a wrong STF in the initial model (here we used a shifted 30 Hz Ricker wavelet as the initial STF). The synthetic data of the inversion result nicely fits the observed waveforms (right column in Fig. 18), implying a successful inversion. The updated STFs in all twelve sources show a high similarity among each other (Fig. 19), indicating high reliability in the estimated STFs.

We also estimated a 2D MASW result by using the same data (Fig. 17c). This 2D result was obtained by combining a total of 16 1D S-wave velocity profiles, which were estimated by a moving boxcar spatial filter of 16 m (Pan et al 2018b). The size of the resulting 2D MASW model is smaller than the MFWI due to the 1D approximation, that means we only estimated one 1D structure every 16 m. The 2D MASW result

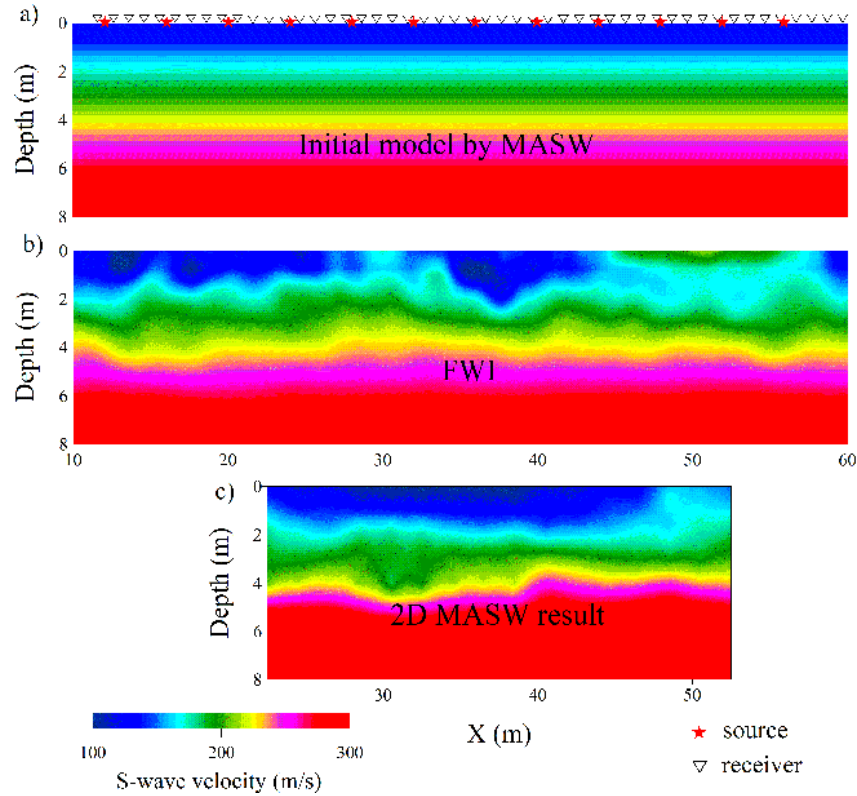


Fig. 17 S-wave velocity model for the Rheinstetten data. a), b) and c) represent the initial model estimated by 1D MASW, the inversion result of MFWI after 52 iterations, and the pseudo-2D MASW result obtained by combining 16 1D profiles, respectively. Asterisks and inverted triangles represent the locations of the sources and the receivers, respectively.

only shows weak lateral variations in the model and is unable to delineate the shape of the trench. Both the FWI and 2D MASW results show that the model has a relatively higher velocity in the right shallow part compared to its left shallow part. This comparison again proves that FWI has a higher resolution compared to MASW.

We compared our S-wave velocity estimated by MFWI to a migrated GPR profile acquired along the same survey line to evaluate our FWI result (Fig. 20). The GPR profile shows a good agreement with the estimated S-wave velocity image. We can clearly see that the velocity contrasts in the S-wave velocity model always match strong events in the GPR profile, especially at the locations where the "V"-shaped low-velocity body exists. The inclined reflector is steeper and deeper in the GPR section compared to the FWI result. This is because the migrated GPR section was derived using a constant-velocity Kirchhoff migration in which the velocity in the trench might be overestimated. Therefore, the reflector corresponding to the trench has probably become steeper and deeper compared to its true location. This is why we only make a qualitative comparison between the FWI result and the migrated GPR section. Both the GPR and FWI results show that the model in its shallow part is more homogeneous on the right side of the trench compared to the left side. Overall, this example proves a fairly high accuracy and reliability of the S-wave velocity model estimated by the sequential strategy.

6 DISCUSSION

The main goal of both MASW and FWI is to extract and exploit information in the seismic waves to reconstruct a subsurface model. MASW only uses the averaged phase velocity involved in the wavefield and neglects information that does not satisfy the plane-wave assumption. Besides, it uses a 1D model to approximate the structure below a multichannel recording system. Thus, MASW features a favorable cost/benefit ratio in using the data (Maurer et al 2010) and is usually able to resolve the subsurface model with a moderate accuracy in a relatively short time. FWI attempts to reconstruct the subsurface model by using the entire wavefield and, thus, obtains a high spatial resolution at the cost of increased computational effort and ill-posedness of the inverse problem. Our results show that MASW is more well-posed compared to FWI, which comes at a cost of losing some useful information in the waveform, such as body waves, scattered surface waves, and some of the high-mode surface waves. Therefore, sequential use of MASW and

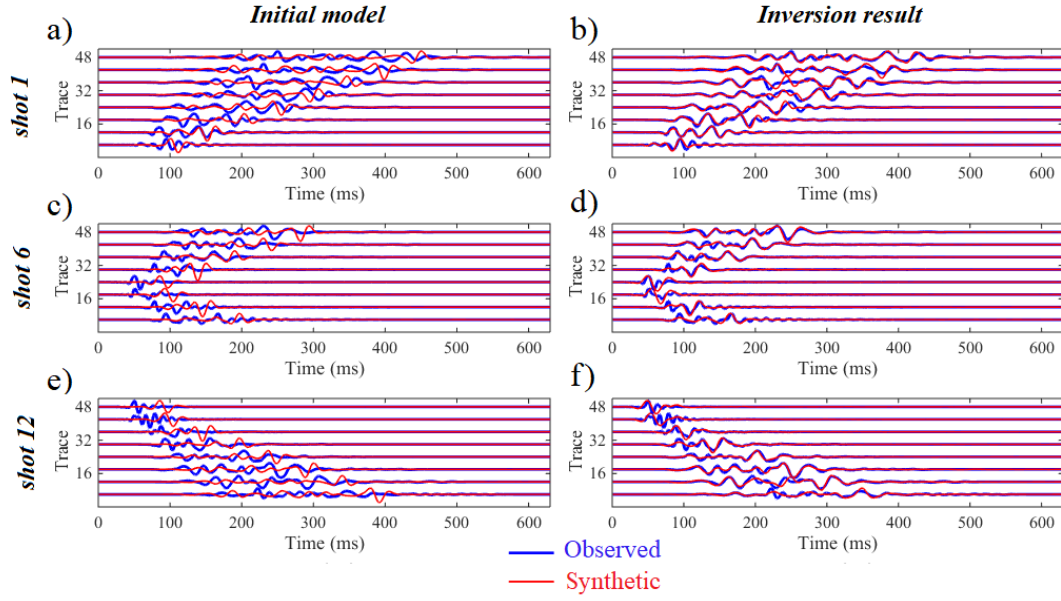


Fig. 18 Comparison between observed (blue) and synthetic (red) waveforms of the initial model (left) and inversion result (right). The three rows denote the comparison of the 1st (top), 6th (middle), and 12th (bottom) shot gather. Blue and red lines represent observed and synthetic waveforms, respectively.

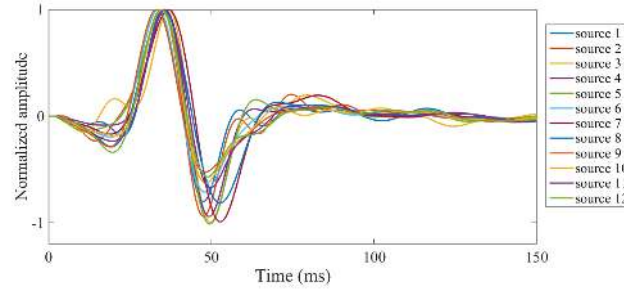


Fig. 19 Estimated source time functions after applying MFWI (up to 60 Hz) to the Rheinstetten data.

FWI provides a cost-effective hierarchical way to reconstruct near-surface structures, while the modified FWI approaches can be used to fill the gap between MASW and classical FWI. Although MASW looks quite well-posed in the numerical example and the waveform simulated with its 1D result can fit the observed data fairly well in the first real-world example, these results do not mean MASW is a panacea in resolving near-surface structures. Both MASW and FWI are mathematically ill-posed, and their solution is nonunique (Foti et al 2009; Menke 2017). Proper constraints and prior information usually benefit the regularization of the inverse problem in both MASW and FWI.

7 CONCLUSIONS

Both multichannel analysis of surface wave (MASW) and full-waveform inversion (FWI) provide ways to use shallow-seismic surface waves in reconstructing near-surface structures. A numerical example was performed to compare the shapes of the objective functions of MASW, classical FWI, and three modified FWI approaches including multiscale FWI, envelope-based FWI, and spectrum-based FWI. It showed that MASW possesses high stability but a relatively low resolution in imaging near-surface structures, while classical FWI behaves just the other way round, and the modified FWI approaches provide an intermediate stability and resolution between MASW and classical FWI. These characteristics were also proven by synthetic inversion tests. They led to the idea that a sequential strategy in which MASW, a (or some) modified FWI approach(es), and classical FWI are progressively used could provide a stable hierarchical way for the high-resolution imaging of near-surface structures. We applied this sequential strategy on two field data sets which were acquired in Olathe, Kansas, USA, and Rheinstetten, Germany, respectively. The sequential-inversion results provided high-resolution subsurface images, which nicely agree with available

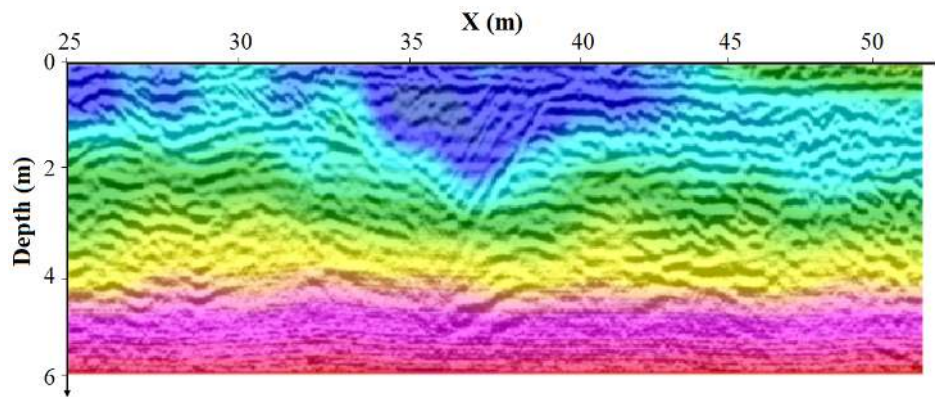


Fig. 20 Comparison between S-wave velocity model estimated by FWI and migrated GPR profile acquired along the survey same line. This figure shares the same color bar with Fig. 17

borehole data and GPR profile. It implies that it is promising to use MASW and FWI sequentially for the high-resolution imaging of shallow-subsurface material.

Acknowledgements The authors would like to thank Dr. Thomas Hertweck for an internal review and Prof. Jianghai Xia for providing the first field data set. The authors also appreciate the editor Michael J. Rycroft and two anonymous reviewers for their helpful and constructive comments. We gratefully acknowledge financial support by the Deutsche Forschungsgemeinschaft (DFG) through CRC 1173.

References

- Aki K, Richards PG (2002) Quantitative seismology. University Science Books
- Aleardi M, Tognarelli A, Mazzotti A (2016) Characterisation of shallow marine sediments using high-resolution velocity analysis and genetic-algorithm-driven 1D elastic full-waveform inversion. *Near Surface Geophysics* 14(5):449–460
- Amrouche M, Yamanaka H (2015) Two-dimensional shallow soil profiling using time-domain waveform inversion. *Geophysics* 80(1):EN27–EN41
- Askari R, Hejazi SH (2015) Estimation of surface-wave group velocity using slant stack in the generalized S-transform domain surface-wave group velocity estimation. *Geophysics* 80(4):EN83–EN92
- Behura J, Snieder R (2013) Virtual real source: Source signature estimation using seismic interferometry. *Geophysics* 78(5):Q57–Q68
- Bergamo P, Socco LV (2014) Detection of sharp lateral discontinuities through the analysis of surface-wave propagation. *Geophysics* 79(4):EN77–EN90
- Bergamo P, Boiero D, Socco LV (2012) Retrieving 2D structures from surface-wave data by means of space-varying spatial windowing. *Geophysics* 77(4):EN39–EN51
- Boaga J, Vignoli G, Cassiani G (2011) Shear wave profiles from surface wave inversion: the impact of uncertainty on seismic site response analysis. *Journal of Geophysics and Engineering* 8(2):162
- Boaga J, Cassiani G, Strobbia CL, Vignoli G (2013) Mode misidentification in Rayleigh waves: Ellipticity as a cause and a cure. *Geophysics* 78(4):EN17–EN28
- Bohlen T (2002) Parallel 3-D viscoelastic finite difference seismic modelling. *Computers & Geosciences* 28(8):887–899
- Bohlen T, Kugler S, Klein G, Theilen F (2004) 1.5D inversion of lateral variation of Scholte wave dispersion. *Geophysics* 69(2):330–344
- Boiero D, Socco LV (2010) Retrieving lateral variations from surface wave dispersion curves. *Geophysical Prospecting* 58(6):977–996
- Boiero D, Bergamo P, Bruno Rege R, Socco LV (2011) Estimating surface-wave dispersion curves from 3D seismic acquisition schemes: Part 11D models. *Geophysics* 76(6):G85–G93
- Borisov D, Modrak R, Gao F, Tromp J (2017) 3D elastic full-waveform inversion of surface waves in the presence of irregular topography using an envelope-based misfit function. *Geophysics* 83(1):1–45
- Bozdağ E, Trampert J, Tromp J (2011) Misfit functions for full waveform inversion based on instantaneous phase and envelope measurements. *Geophysical Journal International* 185(2):845–870
- Brethaudau F, Brossier R, Leparoux D, Abraham O, Virieux J (2013) 2D elastic full-waveform imaging of the near-surface: Application to synthetic and physical modelling data sets. *Near Surface Geophysics* 11(3):307–316
- Brossier R, Operto S, Virieux J (2009) Seismic imaging of complex onshore structures by 2D elastic frequency-domain full-waveform inversion. *Geophysics* 74(6):WCC105–WCC118
- Brossier R, Operto S, Virieux J (2010) Which data residual norm for robust elastic frequency-domain full waveform inversion? *Geophysics* 75(3):R37–R46
- Bunks C, Saleck FM, Zaleski S, Chavent G (1995) Multiscale seismic waveform inversion. *Geophysics* 60(5):1457–1473
- Cercato M (2009) Addressing non-uniqueness in linearized multichannel surface wave inversion. *Geophysical Prospecting* 57(1):27–47
- Chai HY, Phoon KK, Goh SH, Wei CF (2012) Some theoretical and numerical observations on scattering of Rayleigh waves in media containing shallow rectangular cavities. *Journal of Applied Geophysics* 83:107–119
- Chen X (1993) A systematic and efficient method of computing normal modes for multilayered half-space. *Geophysical Journal International* 115(2):391–409

- Dal Moro G, Moura RMM, Moustafa SS (2015) Multi-component joint analysis of surface waves. *Journal of Applied Geophysics* 119:128–138
- Dal Moro G, Moustafa SS, Al-Arifi NS (2018) Improved holistic analysis of Rayleigh waves for single-and multi-offset data: Joint inversion of Rayleigh-wave particle motion and vertical-and radial-component velocity spectra. *Pure and Applied Geophysics* 175(1):67–88
- De Nil D (2005) Characteristics of surface waves in media with significant vertical variations in elasto-dynamic properties. *Journal of Environmental and Engineering Geophysics* 10(3):263–274
- Di Fiore V, Cavuoto G, Tarallo D, Punzo M, Evangelista L (2016) Multichannel analysis of surface waves and down-hole tests in the archeological Palatine Hill area (Rome, Italy): evaluation and influence of 2D effects on the shear wave velocity. *Surveys in Geophysics* 37(3):625–642
- Dokter E, Köhn D, Wilken D, Nil D, Rabbel W (2017) Full-waveform inversion of SH- and Love-wave data in near-surface prospecting. *Geophysical Prospecting* 65:216–236
- Dou S, Ajo-Franklin JB (2014) Full-wavefield inversion of surface waves for mapping embedded low-velocity zones in permafrost. *Geophysics* 79(6):EN107–EN124
- Fichtner A, Kennett BL, Igel H, Bunge HP (2008) Theoretical background for continental- and global-scale full-waveform inversion in the time–frequency domain. *Geophysical Journal International* 175(2):665–685
- Forbriger T (2003) Inversion of shallow-seismic wavefields: I. wavefield transformation. *Geophysical Journal International* 153(3):719–734
- Forbriger T, Groos L, Schäfer M (2014) Line-source simulation for shallow-seismic data. Part 1: Theoretical background. *Geophysical Journal International* 198(3):1387–1404
- Foti S, Comina C, Boiero D, Socco L (2009) Non-uniqueness in surface-wave inversion and consequences on seismic site response analyses. *Soil Dynamics and Earthquake Engineering* 29(6):982–993
- Foti S, Parolai S, Albarello D, Picozzi M (2011) Application of surface-wave methods for seismic site characterization. *Surveys in geophysics* 32(6):777–825
- Foti S, Lai CG, Rix GJ, Strobbia C (2014) Surface wave methods for near-surface site characterization. CRC Press
- Gao L, Pan Y (2016) Acquisition and processing pitfall with clipped traces in surface-wave analysis. *Journal of applied geophysics* 125:1–6
- Gao L, Pan Y (2018) Source signature estimation from multimode surface waves via mode-separated virtual real source method. *Geophysical Journal International* 213(2):1177–1186
- Gao L, Xia J, Pan Y (2014) Misidentification caused by leaky surface wave in high-frequency surface wave method. *Geophysical Journal International* 199(3):1452–1462
- Gao L, Xia J, Pan Y, Xu Y (2016) Reason and condition for mode kissing in MASW method. *Pure and Applied Geophysics* 173(5):1627–1638
- Garofalo F, Foti S, Hollender F, Bard P, Cornou C, Cox BR, Ohrnberger M, Sicilia D, Asten M, Di Giulio G, et al (2016) Interpacific project: Comparison of invasive and non-invasive methods for seismic site characterization. Part I: Intra-comparison of surface wave methods. *Soil Dynamics and Earthquake Engineering* 82:222–240
- Gélis C, Virieux J, Grandjean G (2007) Two-dimensional elastic full waveform inversion using Born and Rytov formulations in the frequency domain. *Geophysical Journal International* 168(2):605–633
- Gilbert JC, Nocedal J (1992) Global convergence properties of conjugate gradient methods for optimization. *SIAM Journal on optimization* 2(1):21–42
- Groos L, Schäfer M, Forbriger T, Bohlen T (2014) The role of attenuation in 2D full-waveform inversion of shallow-seismic body and Rayleigh waves. *Geophysics* 79(6):R247–R261
- Groos L, Schäfer M, Forbriger T, Bohlen T (2017) Application of a complete workflow for 2D elastic full-waveform inversion to recorded shallow-seismic Rayleigh waves. *Geophysics* 82(2):R109–R117
- Haskell NA (1953) The dispersion of surface waves on multilayered media. *Bulletin of the seismological Society of America* 43(1):17–34
- Hayashi K, Suzuki H (2004) CMP cross-correlation analysis of multi-channel surface-wave data. *Exploration Geophysics* 35(0):7–13
- Hestenes MR, Stiefel E (1952) Methods of conjugate gradients for solving linear systems. *Journal of Research of the National Bureau of Standards* 49(6):409–436
- Ikeda T, Tsuji T (2015) Advanced surface-wave analysis for 3D ocean bottom cable data to detect localized heterogeneity in shallow geological formation of a CO₂ storage site. *International Journal of Greenhouse Gas Control* 39:107–118
- Ikeda T, Tsuji T, Matsuoka T (2013) Window-controlled CMP crosscorrelation analysis for surface waves in laterally heterogeneous media. *Geophysics* 78(6):EN95–EN105
- Ikeda T, Matsuoka T, Tsuji T, Nakayama T (2014) Characteristics of the horizontal component of Rayleigh waves in multimode analysis of surface waves. *Geophysics* 80(1):EN1–EN11
- Ivanov J, Miller RD, Xia J, Steeples D, Park CB (2006) Joint analysis of refractions with surface waves: An inverse solution to the refraction-traveltime problem. *Geophysics* 71(6):R131–R138
- Kallivokas L, Fathi A, Kucukcoban S, Stokoe II K, Bielak J, Ghattas O (2013) Site characterization using full waveform inversion. *Soil Dynamics and Earthquake Engineering* 47:62–82
- Ke G, Dong H, Kristensen Å, Thompson M (2011) Modified Thomson–Haskell matrix methods for surface-wave dispersion-curve calculation and their accelerated root-searching schemes. *Bulletin of the Seismological Society of America* 101(4):1692–1703
- Kennett B (1974) Reflections, rays, and reverberations. *Bulletin of the Seismological Society of America* 64(6):1685–1696
- Knopoff L (1964) A matrix method for elastic wave problems. *Bulletin of the Seismological Society of America* 54(1):431–438
- Köhn D, Meier T, Fehr M, Nil D, Auras M (2016) Application of 2D elastic Rayleigh waveform inversion to ultrasonic laboratory and field data. *Near Surface Geophysics* 14(5):461–476
- Kumar J, Naskar T (2017) Resolving phase wrapping by using sliding transform for generation of dispersion curves. *Geophysics* 82(3):V127–V136
- Lin CP, Chang TS (2004) Multi-station analysis of surface wave dispersion. *Soil dynamics and earthquake engineering* 24(11):877–886
- Lin CP, Lin CH, Chien CJ (2017) Dispersion analysis of surface wave testing– SASW vs. MASW. *Journal of Applied Geophysics* 143:223–230
- Liu Y, Teng J, Xu T, Badal J, Liu Q, Zhou B (2017) Effects of conjugate gradient methods and step-length formulas on the multiscale full waveform inversion in time domain: Numerical experiments. *Pure and Applied Geophysics* 174(5):1983–

- 2006
- Lu L, Wang C, Zhang B (2007) Inversion of multimode Rayleigh waves in the presence of a low-velocity layer: numerical and laboratory study. *Geophysical Journal International* 168(3):1235–1246
- Luo Y, Xia J, Miller R, Xu Y, Liu J, Liu Q (2008) Rayleigh-wave dispersive energy imaging using a high-resolution linear Radon transform. *Pure and Applied Geophysics* 165(5):903–922
- Luo Y, Xia J, Liu J, Xu Y, Liu Q (2009) Research on the middle-of-receiver-spread assumption of the MASW method. *Soil Dynamics and Earthquake Engineering* 29(1):71–79
- Maraschini M, Foti S (2010) A monte carlo multimodal inversion of surface waves. *Geophysical Journal International* 182(3):1557–1566
- Masoni I, Brossier R, Virieux J, Boelle J (2013a) Alternative misfit functions for FWI applied to surface waves. In: 75th EAGE Conference & Exhibition incorporating SPE EUROPEC 2013
- Masoni I, Valensi R, Brossier R, Virieux J, Boelle J, Leparoux D, Cote P (2013b) Toward a better full waveform inversion of surface waves. In: 19th European Meeting of Environmental and Engineering Geophysics, EAGE, Expanded Abstracts, vol 19200
- Maurer H, Curtis A, Boerner DE (2010) Recent advances in optimized geophysical survey design. *Geophysics* 75(5):75A177–75A194
- Menke W (2017) The uniqueness of single data function, multiple model functions, inverse problems including the Rayleigh wave dispersion problem. *Pure and Applied Geophysics* 174(4):1699–1710
- Métivier L, Brossier R (2016) The SEISCOPE optimization toolbox: A large-scale nonlinear optimization library based on reverse communication. *Geophysics* 81(2):F1–F15
- Métivier L, Brossier R, Virieux J, Operto S (2013) Full waveform inversion and the truncated newton method. *SIAM Journal on Scientific Computing* 35(2):B401–B437
- Mi B, Xia J, Shen C, Wang L, Hu Y, Cheng F (2017) Horizontal resolution of multichannel analysis of surface waves. *Geophysics* 82(3):EN51–EN66
- Mi B, Xia J, Shen C, Wang L (2018) Dispersion energy analysis of Rayleigh and Love waves in the presence of low-velocity layers in near-surface seismic surveys. *Surveys in Geophysics* 39(2):271288
- Miller R, Xia J, Park C, Ivanov J (1999) Multichannel analysis of surface waves to map bedrock. *The Leading Edge* 18(12):1392–1396
- Mun S, Bao Y, Li H (2015) Generation of Rayleigh-wave dispersion images from multichannel seismic data using sparse signal reconstruction. *Geophysical Journal International* 203(2):818–827
- Nazarian S, Stokoe I, Kenneth H, Hudson W (1983) Use of spectral analysis of surface waves method for determination of moduli and thicknesses of pavement systems. *Transportation Research Record* 930:38–45
- Nguyen TD, Tran KT, McVay M (2016) Evaluation of unknown foundations using surface-based full waveform tomography. *Journal of Bridge Engineering* 21(5):04016013
- Nocedal J, Wright S (2006) Numerical optimization. Springer
- Nuber A, Manukyan E, Maurer H (2017) Optimizing measurement geometry for seismic near-surface full waveform inversion. *Geophysical Journal International* 210(3):1909–1921
- Pan Y, Xia J, Gao L, Shen C, Zeng C (2013a) Calculation of Rayleigh-wave phase velocities due to models with a high-velocity surface layer. *Journal of Applied Geophysics* 96:1–6
- Pan Y, Xia J, Zeng C (2013b) Verification of correctness of using real part of complex root as Rayleigh-wave phase velocity with synthetic data. *Journal of Applied Geophysics* 88:94–100
- Pan Y, Xia J, Xu Y, Gao L (2016a) Multichannel analysis of Love waves in a 3D seismic acquisition system. *Geophysics* 81(5):EN67–EN74
- Pan Y, Xia J, Xu Y, Gao L, Xu Z (2016b) Love-wave waveform inversion for shallow shear-wave velocity using a conjugate gradient algorithm. *Geophysics* 81(1):R1–R14
- Pan Y, Gao L, Bohlen T (2017) Sequential phase-velocity and waveform inversion of shallow-seismic surface waves—A field example for bedrock mapping. In: 23rd European Meeting of Environmental and Engineering Geophysics
- Pan Y, Gao L, Bohlen T (2018a) Time-domain full-waveform inversion of Rayleigh and Love waves in presence of free-surface topography. *Journal of Applied Geophysics* 152:77–85
- Pan Y, Schaneng S, Steinweg T, Bohlen T (2018b) Estimating S-wave velocities from 3D 9-component shallow seismic data using local Rayleigh-wave dispersion curves—a field study. *Journal of Applied Geophysics* 159:532–539
- Park CB, Miller RD, Xia J, et al (1998) Imaging dispersion curves of surface waves on multi-channel record. In: 1998 SEG Annual Meeting, Society of Exploration Geophysicists
- Park CB, Miller RD, Xia J (1999) Multichannel analysis of surface waves. *Geophysics* 64(3):800–808
- Parolai S (2009) Determination of dispersive phase velocities by complex seismic trace analysis of surface waves (CASW). *Soil Dynamics and Earthquake Engineering* 29(3):517–524
- Pei D, Louie JN, Pullammanappallil SK (2008) Improvements on computation of phase velocities of Rayleigh waves based on the generalized R/T coefficient method. *Bulletin of the Seismological Society of America* 98(1):280–287
- Pérez Solano C, Donno D, Chauris H (2014) Alternative waveform inversion for surface wave analysis in 2-D media. *Geophysical Journal International* 198(3):1359–1372
- Piatti C, Socco L, Boiero D, Foti S (2013) Constrained 1D joint inversion of seismic surface waves and P-refraction travel-times. *Geophysical Prospecting* 61(1):77–93
- Plessix R (2006) A review of the adjoint-state method for computing the gradient of a functional with geophysical applications. *Geophysical Journal International* 167(2):495–503
- Plessix R, Mulder W (2004) Frequency-domain finite-difference amplitude-preserving migration. *Geophysical Journal International* 157(1):957–987
- Renalier F, Jongmans D, Savvaidis A, Wathelet M, Endrun B, Cornou C (2010) Influence of parameterization on inversion of surface wave dispersion curves and definition of an inversion strategy for sites with a strong Vs contrast. *Geophysics* 75(6):B197–B209
- Romdhane A, Grandjean G, Brossier R, Rejiba F, Operto S, Virieux J (2011) Shallow-structure characterization by 2D elastic full waveform inversion. *Geophysics* 76(3):R81–R93
- Ryden N, Park CB (2006) Fast simulated annealing inversion of surface waves on pavement using phase-velocity spectra. *Geophysics* 71(4):R49–R58
- Schwab F, Knopoff L (1970) Surface-wave dispersion computations. *Bulletin of the Seismological Society of America* 61:321–344

- Shen C, Wang A, Wang L, Xu Z, Cheng F (2015) Resolution equivalence of dispersion-imaging methods for noise-free high-frequency surface-wave data. *Journal of Applied Geophysics* 122:167–171
- Sloan SD, Peterie SL, Miller RD, Ivanov J, Schwenk JT, McKenna JR (2015) Detecting clandestine tunnels using near-surface seismic techniques. *Geophysics* 80(5):EN127–EN135
- Socco L, Boiero D (2008) Improved monte carlo inversion of surface wave data. *Geophysical Prospecting* 56(3):357–371
- Socco L, Boiero D, Foti S, Wisn R (2009) Laterally constrained inversion of ground roll from seismic reflection records. *Geophysics* 74(6):G35–G45
- Socco L, Foti S, Boiero D (2010) Surface wave analysis for building near surface velocity models: established approaches and new perspectives. *Geophysics* 75(5):A83–A102
- Song X, Tang L, Lv X, Fang H, Gu H (2012) Application of particle swarm optimization to interpret Rayleigh wave dispersion curves. *Journal of Applied Geophysics* 84:1–13
- Strobbia C, Foti S (2006) Multi-offset phase analysis of surface wave data (MOPA). *Journal of Applied Geophysics* 59(4):300–313
- Strobbia C, Laake A, Vermeer P, Glushchenko A (2011) Surface waves: use them then lose them. surface-wave analysis, inversion and attenuation in land reflection seismic surveying. *Near Surface Geophysics* 9(6):503–514
- Tarantola A (1986) A strategy for nonlinear elastic inversion of seismic reflection data. *Geophysics* 51(10):1893–1903
- Tarantola A (1988) Theoretical background for the inversion of seismic waveforms including elasticity and attenuation. *Pure and Applied Geophysics* 128(1-2):365–399
- Tarantola A (2005) Inverse problem theory and methods for model parameter estimation, vol 89. SIAM
- Thomson WT (1950) Transmission of elastic waves through a stratified solid medium. *Journal of applied Physics* 21(2):89–93
- Tran K, McVay M, Faraone M, Horhota D (2013) Sinkhole detection using 2D full seismic waveform tomography. *Geophysics* 78(5):R175–R183
- Tran KT, Sperry J (2018) Application of 2-D full waveform tomography on land-streamer data for assessment of roadway subsidence. *Geophysics* 83(3):1–42
- Tsuji T, Johansen TA, Ruud BO, Ikeda T, Matsuoka T (2012) Surface-wave analysis for identifying unfrozen zones in subglacial sediments S-wave velocity in subglacial sediment. *Geophysics* 77(3):EN17–EN27
- Verachtert R, Lombaert G, Degrande G (2017) Multimodal determination of Rayleigh dispersion and attenuation curves using the circle fit method. *Geophysical Journal International* 212(3):2143–2158
- Vignoli G, Cassiani G (2010) Identification of lateral discontinuities via multi-offset phase analysis of surface wave data. *Geophysical Prospecting* 58(3):389–413
- Vignoli G, Strobbia C, Cassiani G, Vermeer P (2011) Statistical multioffset phase analysis for surface-wave processing in laterally varying media. *Geophysics* 76(2):U1–U11
- Virieux J (1986) P-SV wave propagation in heterogeneous media: velocity-stress finite-difference method. *Geophysics* 51(4):889–901
- Virieux J, Operto S (2009) An overview of full-waveform inversion in exploration geophysics. *Geophysics* 74(6):WCC1–WCC26
- Wang L, Xu Y, Xia J, Luo Y (2015) Effect of near-surface topography on high-frequency Rayleigh-wave propagation. *Journal of Applied Geophysics* 116:93–103
- Watson T (1970) A note on fast computation of Rayleigh wave dispersion in the multilayered elastic half-space. *Bulletin of the Seismological Society of America* 60(1):161–166
- Wu RS, Luo J, Wu B (2014) Seismic envelope inversion and modulation signal model. *Geophysics* 79(3):WA13–WA24
- Xia J (2014) Estimation of near-surface shear-wave velocities and quality factors using multichannel analysis of surface-wave methods. *Journal of Applied Geophysics* 103:140–151
- Xia J, Miller R, Park C (1999) Estimation of near-surface shear-wave velocity by inversion of Rayleigh wave. *Geophysics* 64(4):691–700
- Xia J, Miller RD, Park CB, Tian G (2003) Inversion of high frequency surface waves with fundamental and higher modes. *Journal of Applied Geophysics* 52(1):45–57
- Xia J, Xu Y, Miller RD (2007) Generating an image of dispersive energy by frequency decomposition and slant stacking. *Pure and Applied Geophysics* 164(5):941–956
- Xia J, Xu Y, Miller RD, Zeng C (2010) A trade-off solution between model resolution and covariance in surface-wave inversion. *Pure and Applied Geophysics* 167(12):1537–1547
- Xia J, Xu Y, Luo Y, Miller R, Cakir C, Zeng C (2012) Advantages of using multichannel analysis of Love waves (MALW) to estimate near-surface shear-wave velocity. *Surveys in Geophysics* 33(0):841–860
- Xing Z, Mazzotti A (2018) Two-grid genetic algorithm full waveform inversion of surface waves: Two actual data examples. In: 80th EAGE Conference and Exhibition 2018
- Yamanaka H, Ishida H (1996) Application of genetic algorithms to an inversion of surface-wave dispersion data. *Bulletin of the Seismological Society of America* 86(2):436–444
- Yuan YO, Simons FJ, Bozdağ E (2015) Multiscale adjoint waveform tomography for surface and body waves. *Geophysics* 80(5):R281–R302
- Zeng C, Xia J, Miller R, Tsoflias GP (2011a) Feasibility of waveform inversion of Rayleigh waves for shallow shear-wave velocity using a genetic algorithm. *Journal of Applied Geophysics* 75(0):684–655
- Zeng C, Xia J, Miller RD, Tsoflias GP (2011b) Application of the multiaxial perfectly matched layer (M-PML) to near-surface seismic modeling with Rayleigh waves. *Geophysics* 76(3):T43–T52
- Zeng C, Xia J, Miller RD, Tsoflias GP, Wang Z (2012) Numerical investigation of MASW applications in presence of surface topography. *Journal of Applied Geophysics* 84:52–60
- Zhang SX, Chan LS (2003) Possible effects of misidentified mode number on Rayleigh wave inversion. *Journal of Applied Geophysics* 53(1):17–29